

SIGNATURES OF HOT MOLECULAR HYDROGEN ABSORPTION FROM PROTOPLANETARY DISKS: I. NON-THERMAL POPULATIONS

KERI HOADLEY,¹ KEVIN FRANCE,^{1,2} NICOLE ARULANANTHAM,¹ R.O. PARKE LOYD,¹ AND NICHOLAS KRUCZEK¹

¹*Laboratory for Atmospheric and Space Physics (LASP)
University of Colorado
Space Science Building (SPSC)
3665 Discovery Drive
Boulder, CO 80303, USA*
²*Center for Astrophysical and Space Astronomy (CASA)
University of Colorado
389 UCB
Boulder, CO 80309, USA*

(Received April 7, 2017; Revised July 10, 2017; Accepted November 9, 2018)

Submitted to ApJ

ABSTRACT

The environment around protoplanetary disks (PPDs) regulates processes which drive the chemical and structural evolution of circumstellar material. We perform a detailed empirical survey of warm molecular hydrogen (H₂) absorption observed against H I-Ly α (Ly α : λ 1215.67 Å) emission profiles for 22 PPDs, using archival *Hubble Space Telescope* (HST) ultraviolet (UV) spectra to identify H₂ absorption signatures and quantify the column densities of H₂ ground states in each sightline. We compare thermal equilibrium models of H₂ to the observed H₂ rovibrational level distributions. We find that, for the majority of targets, there is a clear deviation in high energy states ($T_{exc} \gtrsim 20,000$ K) away from thermal equilibrium populations ($T(\text{H}_2) \gtrsim 3500$ K). We create a metric to estimate the total column density of non-thermal H₂ ($N(\text{H}_2)_{\text{nLTE}}$) and find that the total column densities of thermal ($N(\text{H}_2)$) and $N(\text{H}_2)_{\text{nLTE}}$ correlate for transition disks and targets with detectable C IV- pumped H₂ fluorescence. We compare $N(\text{H}_2)$ and $N(\text{H}_2)_{\text{nLTE}}$ to circumstellar observables and find that $N(\text{H}_2)_{\text{nLTE}}$ correlates with X-ray and FUV luminosities, but no correlations are observed with the luminosities of discrete emission features (e.g., Ly α , C IV). Additionally, $N(\text{H}_2)$ and $N(\text{H}_2)_{\text{nLTE}}$ are too low to account for the H₂ fluorescence observed in PPDs, so we speculate that this H₂ may instead be associated with a diffuse, hot, atomic halo surrounding the planet-forming disk. We create a simple photon-pumping model for each target to test this hypothesis and find that Ly α efficiently pumps H₂ levels with $T_{exc} \geq 10,000$ K out of thermal equilibrium.

Keywords: protoplanetary disks — molecular processes — line: profiles — stars: variables: T Tauri, Herbig Ae/Be — techniques: spectroscopic — ultraviolet: general

arXiv:1707.03449v1 [astro-ph.SR] 11 Jul 2017

1. INTRODUCTION

Protoplanetary disks (PPDs) are thought to provide the raw materials that form protoplanets and drive planetary systems to their final architectures (Lubow et al. 1999; Lubow & D’Angelo 2006; Armitage et al. 2003; Brown et al. 2009; Woitke et al. 2009; Ayliffe & Bate 2010; Dullemond & Monnier 2010; Beck et al. 2012). The presence of significant amounts of gas in the disk is a defining quality of PPDs, where the earliest stages are assumed to have the canonical interstellar medium (ISM) gas-to-dust ratio $\sim 100:1$ (e.g., Frisch et al. 1999; Schneider et al. 2015). The gas content in PPDs controls essential processes tied to the formation and evolution of planetary systems, including dust grain growth (through the coupling of gas and dust dynamics), angular momentum transport, and thermal and chemical balance of the disk as it evolves (Weidenschilling 1977; Alexander & Armitage 2007; Woitke et al. 2009; Youdin 2011; Levison et al. 2015). However, over timescales of a few Myr, PPDs lose their massive gas disk, evolving to gas-sparse debris disks (with gas-to-dust ratios $\sim 0:1$; Alexander et al. 2014; Gorti et al. 2015). The dispersal of the gas-rich disk is likely driven by a number of different physical processes throughout the PPD lifetime, ranging from photoevaporation of gas through thermal winds (for example, an atomic wind: e.g., Owen et al. 2010; a fully-ionized wind: e.g., Alexander et al. 2006; and/or a slow molecular wind: see review by Alexander et al. 2014) or magnetohydrodynamic (MHD) winds (e.g. Ferreira et al. 2006; Bai 2016), to giant planet formation accreting and clearing gas remaining in a dust gap (Lin & Papaloizou 1986; Dodson-Robinson & Salyk 2011; Zhu et al. 2011; Dong et al. 2015; Owen 2016). Probing the physical mechanisms that drive the dispersal of gas from PPDs is critical for inferring when, where, and how planet-forming disks lose their massive gas reservoir. In turn, these properties inform us of the physical and chemical environment in which planets form throughout the PPD lifetime.

Internal radiation from the proto-stellar source can play an important role in determining the chemical and physical state of the gas-rich PPD (Kamp & Dullemond 2004; Nomura 2004; Nomura et al. 2007; Öberg et al. 2010; Bethell & Bergin 2011). Ultraviolet (UV) and X-ray radiation, which are created by hot gas accretion onto and activity in the protostellar atmosphere, can effectively enhance the populations of rovibrationally-excited molecules, which create pathways for molecular dissociation (e.g. Glassgold & Najita 2001; Bergin et al. 2004; Gorti & Hollenbach 2004; Glassgold et al. 2004; Kamp et al. 2005; Dullemond et al. 2007; Güdel et al. 2007; Kastner et al. 2016). High-energy radiation may also help heat and regulate chemical processes in the disk atmosphere, leading to the production of atomic and molecular by-products (e.g. Salyk et al. 2008; Walsh et al. 2015; Ádámkóvics et al. 2016). Hot molecules can

be swept up into thermal winds over the disk lifetime (Alexander et al. 2006; Gorti & Hollenbach 2009; Owen et al. 2010; Owen 2016), leading to the dispersal of the disk from the inside-out.

Molecular hydrogen (H_2) has been measured to be 10^4 times more abundant than other molecules (e.g., CO) in the warm regions of PPDs (France et al. 2014a), and large quantities of H_2 in the disk allow the molecule to survive at hot temperatures ($T(H_2) \sim 1000 - 5000$ K), shielding against collisional- and photo-dissociation (Williams & Murdin 2000; Beckwith et al. 1978, 1983). The properties of H_2 make it a reliable diagnostic of the spatial and structural behavior of warm molecules probed in and around PPDs (Ardila et al. 2002; Herczeg et al. 2004), as it is expected to trace residual amounts of gas in disks throughout their evolution ($\Sigma_{H_2} \sim 10^{-6}$ g cm^{-2} ; e.g., France et al. 2012b).

However, H_2 is notoriously difficult to observe in PPDs; cold H_2 ($T(H_2) \sim 10$ K) does not radiate and, due to its lack of a permanent dipole (Sternberg 1989), ro-vibrational transitions of H_2 in the IR are dominated by weak, quadrupole transitions. Therefore, it has been easier to trace other molecular constituents of the inner disk, such as CO and HD, to interpret the behavior of the underlying H_2 reservoir (e.g., Salyk et al. 2011; Brown et al. 2013; Banzatti & Pontoppidan 2015; McClure et al. 2016). Most IR studies of H_2 in PPDs have been detections of shocked (hot) H_2 in collimated jets or streams (Bary et al. 2003; Beck et al. 2012; Arulanantham et al. 2016).

The far ultraviolet (FUV: $\lambda\lambda 912 - 1700$ Å) offers the strongest transition probabilities for dipole-allowed electronic transitions of H_2 photo-excited by UV photons, specifically absorption avenues coincident with H I- $Ly\alpha$ ($\lambda 1215.67$ Å) photons, which are generated near the protostellar surface (France et al. 2012b; Schindhelm et al. 2012) and make up $\sim 90\%$ of the FUV flux in a typical T Tauri system (France et al. 2014b). Warm H_2 ($T \geq 1000$ K) can absorb $Ly\alpha$ photons, exciting the molecule up to either the Lyman ($2p\sigma B^1\Sigma_u^+$) or Werner ($2p\pi C^1\Pi_u$) electronic bands. Because of the large dipole-allowed transition probabilities ($A_{ul} \sim 10^8$ s $^{-1}$; Abgrall et al. 1993a,b), H_2 in these electronic states will decay instantaneously in a fluorescent cascade down to one of many different rovibration levels in the ground electronic state ($X^1\Sigma_g^+$; Herczeg et al. 2002). Each fluorescence transition results in the discrete emission of a FUV photon, whose frequency depends on the electronic-to-ground state transition. We observed hundreds of these features throughout the FUV with the *Hubble Space Telescope* (*HST*) from $\lambda\lambda 1150 - 1700$ Å (see Herczeg et al. 2002; France et al. 2012b). This process predominantly favors regions where warm molecules reside in disks (Nomura & Millar 2005; Nomura et al. 2007; Ádámkóvics et al. 2016). The characterization of H_2 emission from PPDs has provided complimentary results to high-resolution IR-CO surveys probing PPD

evolution (e.g. Brown et al. 2013; Banzatti & Pontoppidan 2015).

We can also observe the excitation leg of the fluorescence process via H₂ absorption lines incident on the broad Ly α emission line in PPD systems. Several studies have looked to characterize and relate the H₂ absorption features within protostellar Ly α wings to fluorescent populations tied to the behavior of the inner disk material. Yang et al. (2011) detected the first signatures of Ly α -H₂ absorption in DF Tau and V4046 Sgr. They found that, for V4046 Sgr, which hosts a circumbinary disk with a relatively face-on inclination angle ($i_{disk} \sim 35^\circ$), the H₂ would have to be pumped near the accretion shock to explain how H₂ absorption features are detectable in the sightline. France et al. (2012a) performed an extensive study on warm molecules in the disk environment of AA Tau and were the first to empirically derive H₂ column densities from absorption features within the Ly α red stellar wing. The lower energy states of H₂ could be described by a warm thermal population ($T(\text{H}_2) \sim 2500 \text{ K} \pm 1000 \text{ K}$) consistent with H₂ fluorescence emission from the inner disk. They noticed that, for high excitation temperature states of H₂ ($T_{exc} \geq 20,000 \text{ K}$), column densities deviated significantly from thermal distributions, providing the first hint that there may be additional excitation mechanisms in the disk atmosphere pumping H₂ out of local thermodynamic equilibrium (LTE).

The behavior of these non-thermal states may provide clues about the mechanisms that drive molecules out of LTE and, potentially, the dispersal of gas from planet-forming disks. In the first paper of this study, we perform a quantitative, empirical survey of H₂ absorption observed against the Ly α stellar emission profiles of 22 PPD hosts. We aim to characterize the physical state of the gas in each sightline and learn how various stellar and disk mechanisms contribute to the excitation of non-thermal H₂ states. In Section 2, we present the archival observations used to perform this study. In Section 3, we describe the methodology of extracting H₂ absorption features from each Ly α emission profile and quantifying the column densities of each H₂ rovibrational level. In Section 4, we present results from fitting thermal models to the column density rotation diagrams for each target and what those results reveal about the non-thermal density distributions of H₂ in each sightline. In Section 5, we compare our results to observed disk and stellar properties, which probe different excitation mechanisms that may help explain excesses in non-thermal populations of H₂. We take all the evidence provided by this empirical study to infer the most likely location of H₂ absorption in the disk atmosphere. Finally, in Section 6, we conclude our paper with our major findings and future work that may help clarify open questions left unresolved by this study. In a follow-up study (Paper II), we will consider where the H₂ populations originate in the circumstellar environment. Additional plots and

details about our absorption and thermal models are provided in the Appendix.

2. TARGETS AND OBSERVATIONS

Our target list is derived from McJunkin et al. (2014), who analyzed the reddening of the HI-Ly α profiles of 31 young stellar systems to create a comprehensive list of interstellar dust extinction estimates along each sight line. Of the 31 original targets, 22 of the protostellar targets showed signs of H₂ absorption in the Ly α profiles. All of these observations have been described previously in studies of H₂ (e.g. France et al. 2012b; Hoadley et al. 2015), hot gas (e.g. Ardila et al. 2013), and UV radiation (e.g. France et al. 2014b). Several of the targets are known binaries or multiples (DF Tau: Ghez et al. 1993; HN Tau, RW Aur, and UX Tau: Correia et al. 2006; AK Sco and HD 104237 are spectroscopic binaries: Gómez de Castro 2009; Böhm et al. 2004; and V4046 Sgr is a short-period binary, which acts as a point source for most applications: Quast et al. 2000), and only the primary stellar component is observed within the aperture. The majority of the targets are observed within the Taurus-Auriga and η Chamaeleontis star-forming regions, with distances of 140 and 97 pc, respectively. Young stars observed in these star-forming regions have ages ranging a few Myr, while field pre-main sequence stars (e.g. TW Hya, V4046 Sgr) have ages range between 10 – 30 Myr. The majority of these targets have age ranges comparable to the depletion timescale of gas and circumstellar dust via accretion processes (Hernández et al. 2007; Fedele et al. 2010), making them ideal candidates for understanding the abundance and physical state of H₂ at a variety of PPD evolutionary stages. Table 1 presents relevant stellar and disk properties. All observations of the stellar Ly α profiles were taken either with the Cosmic Origins Spectrograph (COS) or Space Telescope Imaging Spectrograph (STIS) aboard the *Hubble Space Telescope* (HST).

2.1. COS Observations

Each PPD spectrum collected with HST/COS was taken either during the Disk, Accretion, and Outflows (DAO) of Tau Guest Observing (GO) program (PID 11616; PI: G. Herczeg) or COS Guaranteed Time Observing (PIDs 11533 and 12036; PI: J. Green). Each spectrum was observed with the medium-resolution far-UV modes of the spectrograph (G130M and G160M ($\Delta v \approx 18 \text{ km s}^{-1}$ at Ly α); Green et al. 2012). Multiple central wavelength positions were included to minimize fixed-pattern noise. The COS data were processed using the COS calibration pipeline (CALCOS) and were aligned and co-added with the procedure described by Danforth et al. (2010). By design, COS is a slitless spectrograph, allowing the full $2''.5$ field of view through the instrument. This means the instrument is exposed to strong contamination from geocoronal Ly α (Ly α_{\oplus}). To

Table 1. Target Properties

Target	Spectral Type	Disk Type ^a	Distance (pc)	L_* (L_\odot)	M_* (M_\odot)	\dot{M} ($\times 10^{-8} M_\odot \text{ yr}^{-1}$)	i_{disk} ($^\circ$)	Ref. ^b
AA Tau	K7	P	140	0.71	0.80	0.33	75	2, 4, 7, 12, 16, 52, 53
AB Aur	A0	T	140	46.8	2.40	1.80	22	19, 39, 49, 50, 52, 53
AK Sco	F5	P	103	7.59	1.35	0.09	68	18, 20, 34, 57
BP Tau	K7	P	140	0.925	0.73	2.88	30	7, 12, 38, 52, 53
CS Cha	K6	T	160	1.32	1.05	1.20	60	21, 35, 40, 54
DE Tau	M0	T	140	0.87	0.59	2.64	35	7, 10, 12, 52, 53
DF Tau A	M2	P	140	1.97	0.19	17.70	85	7, 10, 52, 53
DM Tau	M1.5	T	140	0.24	0.50	0.29	35	16, 29, 32, 52, 53
GM Aur	K5.5	T	140	0.74	1.20	0.96	55	7, 16, 32, 52, 53
HD 104237	A7.5	T	116	34.7	2.50	3.50	18	19, 23, 31, 45
HD 135344B	F3	T	140	8.13	1.60	0.54	11	19, 22, 31, 42, 57
HN Tau A	K5	P	140	0.19	0.85	0.13	40	6, 7, 12, 52, 53
LkCa 15	K3	T	140	0.72	0.85	0.13	49	12, 29, 32, 52, 53
RECX-11	K4	P	97	0.59	0.80	0.03	70	13, 24, 47, 55
RECX-15	M2	P	97	0.08	0.40	0.10	60	13, 14, 15, 55
RU Lup	K7	T	121	0.42	0.80	3.00	24	25, 30, 36, 41, 56
RW Aur A	K4	P	140	2.3	1.40	3.16	77	5, 9, 11, 12, 17, 52, 53
SU Aur	G1	T	140	9.6	2.30	0.45	62	1, 3, 8, 11, 12, 52, 53
SZ 102	K0	T	200	0.01	0.75	0.08	90	26, 37, 43, 48
TW Hya	K6	T	54	0.17	0.60	0.02	4	27, 30, 42, 51, 56
UX Tau A	K2	T	140	3.5	1.30	1.00	35	12, 32, 52, 53
V4046 Sgr	K5	T	83	0.5+0.3	0.86+0.69	1.30	34	28, 33, 44, 46

^aDisk Type is defined by either the detection of small dust grain depletion in the inner disk regions, resulting in disk holes or gaps, or the degree of dust settling in the disk, or both; PPDs can be categorized using an observable n_{13-31} , which is defined by the slope in the spectral energy distribution (SED) flux between 13 μm and 31 μm (Furlan et al. 2009): P = primordial ($n_{13-31} < 0$); T = transitional ($n_{13-31} > 0$).

^b**References:** (1) Akeson et al. (2002), (2) Andrews & Williams (2007), (3) Bertout et al. (1988), (4) Bouvier et al. (1999), (5) Eisner et al. (2007), (6) France et al. (2011), (7) Gullbring et al. (1998), (8) Gullbring et al. (2000), (9) Hartigan et al. (1995), (10) Johns-Krull & Valenti (2001), (11) Johns-Krull et al. (2000), (12) Kraus & Hillenbrand (2009), (13) Lawson et al. (2004), (14) Luhman (2004), (15) Ramsay Howat & Greaves (2007), (16) Ricci et al. (2010), (17) White & Ghez (2001), (18) van den Ancker et al. (1998), (19) van Boekel et al. (2005), (20) Alencar et al. (2003), (21) Lawson et al. (1996), (22) Lyo et al. (2011), (23) Feigelson et al. (2003), (24) Lawson et al. (2001), (25) Herczeg et al. (2005), (26) Comerón & Fernández (2010), (27) Webb et al. (1999), (28) Quast et al. (2000), (29) Hartmann et al. (1998), (30) Herczeg & Hillenbrand (2008), (31) Garcia Lopez et al. (2006), (32) Andrews et al. (2011), (33) France et al. (2012a), (34) Gómez de Castro (2009), (35) Espaillat et al. (2007), (36) Stempels et al. (2007), (37) Comerón et al. (2003), (38) Simon et al. (2000), (39) Tang et al. (2012), (40) Espaillat et al. (2011), (41) Stempels & Piskunov (2002), (42) Pontoppidan et al. (2008), (43) Coffey et al. (2004), (44) Rodriguez et al. (2010), (45) Grady et al. (2004), (46) Rosenfeld et al. (2012a), (47) Ingleby et al. (2011), (48) Hughes et al. (1994), (49) Hashimoto et al. (2011), (50) Donehew & Brittain (2011), (51) Rosenfeld et al. (2012b), (52) Bertout et al. (1999), (53) Loinard et al. (2007), (54) Luhman (2004), (55) Mamajek et al. (1999), (56) van Leeuwen (2007), (57) Grady et al. (2009).

mitigate this contamination, we mask the central $\sim 2 \text{ \AA}$ of the Ly α spectra.

2.2. STIS Observations

Several targets either exceeded the COS bright-object limit or had archival STIS observations available with the desired far-UV bandpass and resolution (AB Aur, HD 104237, TW Hya). The archival data were obtained with the STIS medium-resolution grating mode (G140M

($\Delta v \approx 30 \text{ km s}^{-1}$ between 1150 – 1700 \AA): Kimble et al. (1998); Woodgate et al. (1998)), while the COS-bright objects were observed with the echelle medium-resolution mode (E140M ($\Delta v \approx 7 \text{ km s}^{-1}$ between 1150 – 1700 \AA)). The STIS echelle spectra were processed using echelle calibration software developed for the STIS StarCAT catalog (Ayres 2010). Unlike COS, STIS has a small slit aperture ($0''.2 \times 0''.2$), so the Ly α_\oplus signal is

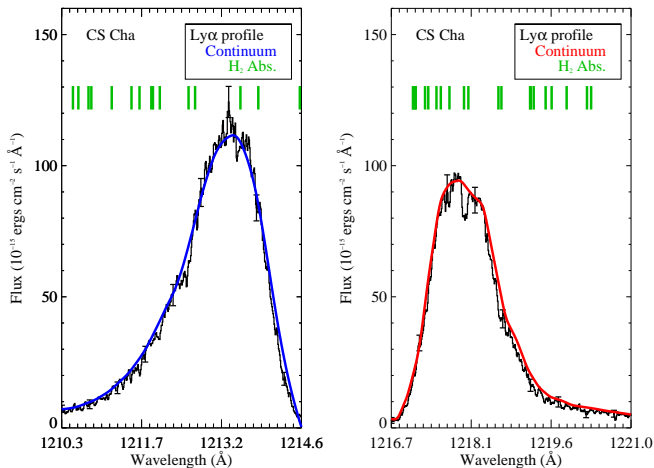


Figure 1. The stellar Ly α wings for one target (CS Cha) in our survey. Within the wings themselves, absorption signatures can be seen. The mean flux array over the Ly α profile is selected to minimize contamination from the absorption features and trace the shape of the Ly α wings. The mean flux array is smoothed (and shown in blue over the blue Ly α wing and red over the red Ly α wing), and the observed line profile is divided by the mean flux array to create relative absorption spectra across the Ly α profile. H₂ absorption transitions are identified with green hashes and properties about each transition are shown in Table 2.

weaker; nonetheless, we remove the inner region of the Ly α profile ($\sim 0.5 - 2 \text{ \AA}$) for consistency among all the data.

3. LY α NORMALIZATION AND ABSORPTION LINE SPECTROSCOPY

We identify absorption signatures of H₂ in each sightline by creating transmission spectra of the stellar Ly α profiles of each PPD host. We treat each Ly α profile as a “continuum” source and normalize the emission feature, such that $I_{Ly\alpha} \approx 1.0$. We create a grid of 5 – 10 unique spectral bins from $\lambda\lambda 1216.5 - 1221.5 \text{ \AA}$ (or $\lambda\lambda 1210.0 - 1215.0 \text{ \AA}$ for the blue wing component), which are each selected by hand to avoid molecular absorption features. Each grid bin is defined over 0.35 \AA , to both smooth the Ly α emission feature and avoid washing out the H₂ absorption features. Within each grid, we measure the mean and standard deviation along the Ly α profile and store them in binned flux and error arrays. We smooth each flux array with a boxcar function of size 0.5 \AA over the Ly α bandpass and normalize the Ly α profile with this smoothed grid. An example of the smoothed grid array over the Ly α profile for one of our survey targets is shown in Figure 1, and all Ly α profiles are presented in Appendix 1.

Figure 2 presents the normalized Ly α spectra for 6 targets, shown in order of inclination angle (edge-on targets on the bottom, and face-on targets towards the top). The effective “continuum” levels of the normal-

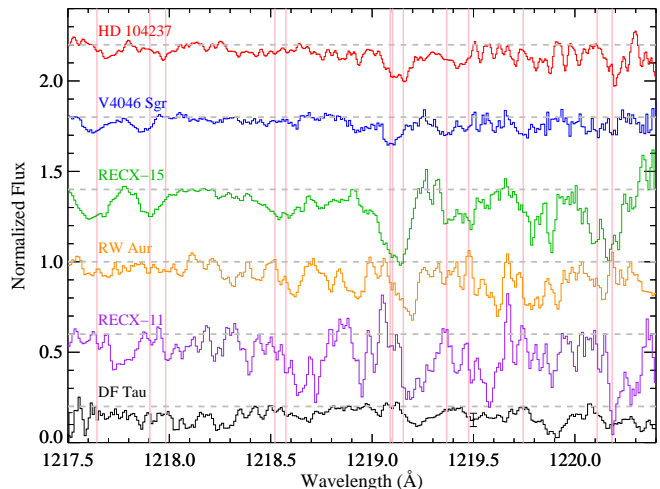


Figure 2. The normalized absorption spectra for 6 targets in our survey, ordered by increasing disk inclination angle (i_{disk}) from the top-down (11° , 34° , $\sim 60^\circ$, $\sim 70^\circ$, 77° , and 85° , respectively) from $\lambda\lambda 1217.5 - 1220.5 \text{ \AA}$. Each target is shown in a different color and offset from $I_{Ly\alpha} \approx 1.0$, which is shown with the dashed gray horizontal line. The laboratory wavelengths of H₂ absorption features considered in this study are shown with solid pink vertical lines. For each target, absorption profiles are expected to be red-shifted by $v \sin i_{disk} \approx 2, 0, 10, 15, 19,$ and 16 km s^{-1} , respectively (Nguyen et al. 2012; Woitke et al. 2013; Quast et al. 2000), which correspond to $\Delta\lambda \sim 0.01, 0.00, 0.04, 0.06, 0.08,$ and 0.07 \AA .

ized Ly α flux profiles are indicated by the gray dashed lines of each spectrum, and relative flux minima with full width half maximum (FWHM) greater than the spectral resolution of the data are interpreted as absorption features. We highlight where H₂ absorption features are expected to reside in the spectrum with solid pink lines. For the edge-on targets (DF Tau, RECX-11, RW Aur), we see the absorption features appear systematically red-shifted. For face-on targets (V4046 Sgr and HD 104237), the position of the absorption features matches the expected laboratory wavelength of H₂. The observed red-shift in H₂ absorption is expected to fall within corrections made for the radial velocity ($v \sin i_{disk}$) of each target and the uncertainty in the COS wavelength solution ($\Delta v \sim 15 \text{ km s}^{-1}$). Additionally, there are several absorption features seen in more than one target that do not coincide with marked H₂ features, most notably around 1218.35 \AA and 1219.80 \AA . As a first-order check that all H₂ and additional absorption features are not artifacts of instrument systematic errors (e.g., gain sag signature from the COS MAMA detector), we compare the Ly α normalized absorption profiles from two observing modes ($\lambda 1291$ and $\lambda 1327$) of the G130M grating for RECX-15 and find that absorption features appear in both observing modes, giving confidence that these features are real. We will attempt to identify unknown

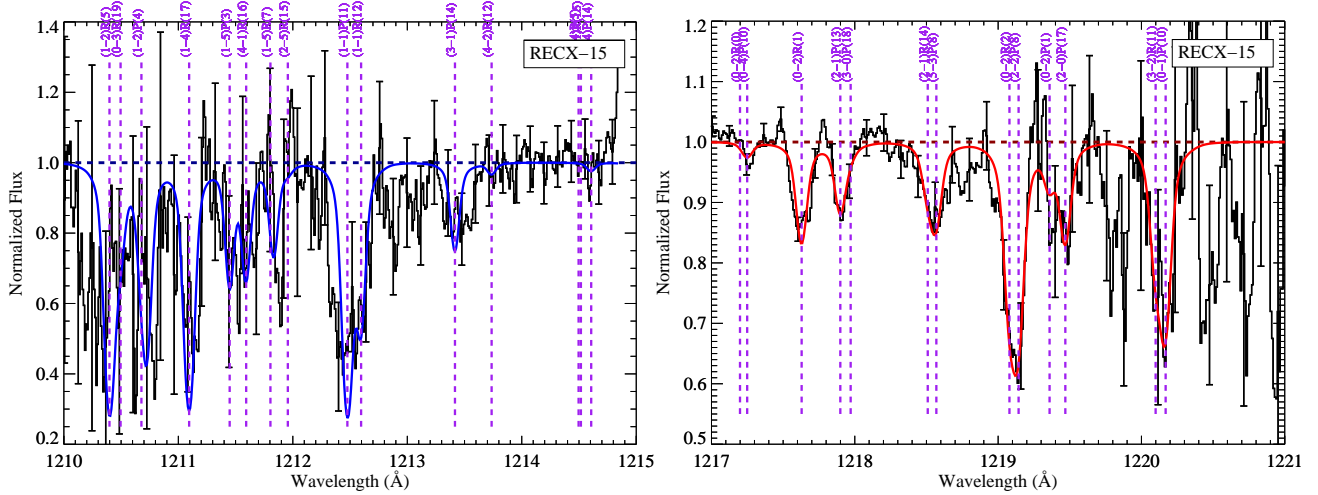


Figure 3. The best-fit H_2 absorption spectrum for RECX-15, assuming $b_{\text{H}_2} = 5 \text{ km s}^{-1}$ is shown in blue (*left*) and red (*right*) over the data (black). Prominent absorption features are labeled in each figure. Table 2 lists all H_2 features considered for the fit, and Table 3 presents best-fit thermal model parameters, given the distribution of rovibrational column densities derived from these absorption line fits.

features and verify that these features are real, performing the same check on two different observing modes of COS, in Paper II.

We create a multi-component H_2 fitting routine to measure the column density in the absorption lines probed within the red and blue stellar wings of $\text{Ly}\alpha$, pumped either into the Lyman or Werner electronic band system. We create intrinsic line profiles from the molecular transition properties (listed in Table 2) to infer the individual column densities probed in each observed rovibrational $[v, J]$ level, as well as the average H_2 population properties ($T(\text{H}_2)$, b_{H_2} , $N(\text{H}_2)$). The modeled b-value is fixed in all synthetic absorption spectra to replicate the thermal width of a warm bulk population of H_2 ($T(\text{H}_2) \geq 2500 \text{ K}$) in the absence of turbulent velocity broadening. Each line profile is co-added in optical depth space, and a transmission curve is created, which is convolved with either the COS LSF (Kriss 2011) or a Gaussian LSF at the STIS resolving power, prior to comparison with the observed $\text{Ly}\alpha$ spectra. Each best-fit, multi-absorption feature H_2 model is then determined using the MPFIT routine (Markwardt 2009). Initial conditions for each transmission curve were first determined by manually fitting each H_2 spectrum. To remove bias introduced by the choice of initial conditions, a grid of initial parameters was searched for all sampled absorption spectra. The only parameter allowed to float continuously for all targets was the velocity shift of the line centers of the H_2 absorption features, v_r .

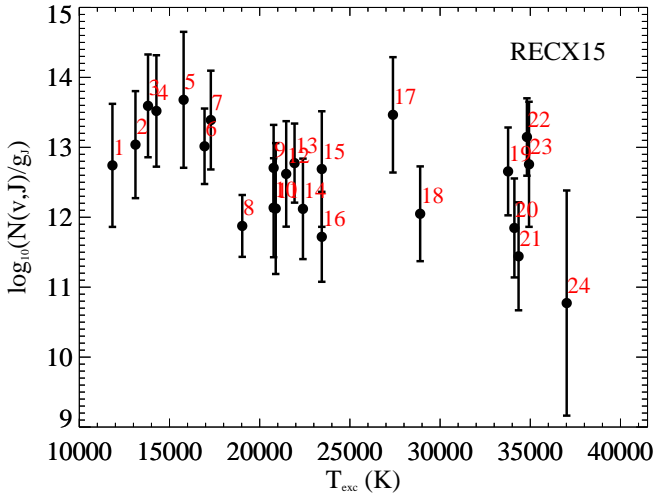


Figure 4. The rotation diagram produced for H_2 ground state rovibrational levels probed in the protostellar $\text{Ly}\alpha$ profile of RECX-15. The column density in each rovibrational state is determined from the H_2 absorption line fits shown in Figure 3. Each label number in the plot corresponds with the following H_2 transitions: 1. (0-2)R(1); 2. (1-2)P(4); 3. (1-2)R(5); 4. (0-1)P(10); 5. (1-1)P(11); 6. (2-2)P(8); 7. (1-1)R(12); 8. (2-1)P(13); 9. (3-1)P(14); 10. (2-1)R(14); 11. (3-2)R(11); 12. (2-0)P(17); 13. (5-3)P(8); 14. (4-2)R(12); 15. (4-1)R(16); 16. (3-0)P(18); 17. (1-5)P(3); 18. (0-4)P(10); 19. (2-5)P(11); 20. (0-3)R(19); 21. (1-4)P(14); 22. (1-4)R(17); 23. (2-4)P(18); 24. (2-5)R(15).

Figure 3 shows the normalized H_2 absorption profiles in the blue and red $\text{Ly}\alpha$ emission profiles of RECX-15, with the best-fit synthetic H_2 absorption profiles overlaid in blue (*left*) and red (*right*) and labeled with the H_2 transition information. Figure 4 presents the resulting rotation diagram of H_2 ground state rovibrational in the sightline of RECX-15. All other synthetic H_2 absorption models and rotation diagrams are presented in Figure 2. The best-fit column densities and standard de-

viations are plotted in rotational diagrams against the rovibrational energy level ($T_{exc} = E''/k_B$). Each H₂ level is statistically-weighted to correct for ortho- and para-H₂ species, such that $g_J = (2S + 1)(2J + 1)$, for $S = 0$ (para-H₂) and $S = 1$ (ortho-H₂).

We check our methodology by comparing our results to France et al. (2012a), who performed a similar procedure for the Ly α absorption spectrum of AA Tau. Figure 5 (left) presents the H₂ absorption spectrum for the red Ly α spectrum of AA Tau, as performed in this study. Figure 5 (right) shows the H₂ rotation diagram for AA Tau determined in this study (purple) and France et al. (2012a) (black). The H₂ column densities in both studies agree within the error bars determined by the multi-component fit. Our study identified two additional H₂ absorption features not fit in France et al. (2012a) (H₂[0,19], pumped by $\lambda 1217.41$ Å, and H₂[6,3], pumped by $\lambda 1217.49$ Å). These transitions were important to capture, as observing and characterizing high energy H₂ ground states in PPD environments is a key motivation for this study.

4. ANALYSIS & RESULTS

We aim to characterize the behavior of the rovibrational H₂ populations identified in the PPD host Ly α spectra and estimate the total thermal and non-thermal column densities ($N(\text{H}_2)$ and $N(\text{H}_2)_{\text{nLTE}}$) of H₂ in each sightline.

Figure 6 presents the rotation diagrams for all targets in this survey. We split the sampled sightlines by PPD evolution phase, which we define by the behavior of excess infrared (dust) emission from 13 – 31 μm (Furlan et al. 2009). Primordial PPDs are thought to be “young” disks with very little evidence of dust evolution and grain growth, meaning planet formation is either starting or in very early stages. Transitional disks are viewed as “older” disks where proto-planets have formed and are evolving, since the observed infrared dust distributions point to the build-up of larger dust grains. Transition disks also (typically) harbor one or more large dust cavities that indicate significant evolution of the disk material (e.g., see Strom et al. 1989; Takeuchi & Artymowicz 2001; Calvet et al. 2002, 2005; Espaillat et al. 2007). To explore the behavior of H₂ populations simultaneously in all PPD sightlines, we normalize each H₂ rotation diagram to the column density in the [$v = 2, J = 1$] level. We include thermal models of warm/hot distributions of H₂ populations, drawn through the normalization rovibrational level [$v = 2, J = 1$], which range from the expected thermal populations of fluorescent H₂ in PPDs (Herczeg et al. 2002, 2006; France et al. 2012b; Hoadley et al. 2015) to the dissociation limit of the molecule (red dashed line for $T_{diss} \approx 4500$ K; Shull & Beckwith 1982; Williams & Murdin 2000).

Despite the evolutionary differences in the dust distributions between the two PPD types, primordial and

transitional PPD sightlines appear to show very similar H₂ rovibrational behaviors. Thermal distributions for $T(\text{H}_2) < 3300$ K do not appear to describe the behavior of H₂ rovibration levels for $T_{exc} > 23,000$ K, but a thermal distribution of H₂ at or near the dissociation limit of the molecule does appear to be consistent with the lowest column densities of rovibrational H₂ at 23,000 K $< T_{exc} < 40,000$ K. Still, we note that the majority of H₂ levels are significantly pumped, sometimes by as much as 4 dex, above the thermal distribution of H₂.

Additionally, we see a striking behavior in the distribution of H₂ rovibrational levels with $T_{exc} > 20,000$ K. At $T_{exc} \sim 20,000$ K, there is an abrupt upturn, or “knee,” away from the thermal distributions and an increase in rovibrational column density for higher excitation temperature states by $\gtrsim 1$ dex. This “knee” appears to repeat around $T_{exc} \sim 25,500$ K and 31,000-32,000 K. This behavior, specifically between the “knees” at $T_{exc} \sim 25,500$ and 32,000 K, may be a result of under-sampling the distribution of highly-energetic H₂ with ground state energies in this range.

Non-thermal pumping mechanisms include many complex processes, which are challenging and computationally-expensive to model simultaneously; Nomura & Millar (2005) and Nomura et al. (2007) show how many mechanisms, such as chemical processes (resulting in the destruction and formation of H₂), FUV/X-ray pumping, and dust grain formation and size distributions in PPD atmospheres (Habart et al. 2004; Aikawa & Nomura 2006; Nomura & Nakagawa 2006; Fleming et al. 2010), affect the population ratios of H₂ and pump H₂ populations out of thermal equilibrium. However, Nomura & Millar (2005) also show that small changes in any of these processes can have dramatic effects on the final structure of H₂ rovibrational levels. Since we do not sample the full suite of [v, J] ground states in this absorption line study, we do not attempt to model multiple, non-thermal mechanisms in the hope of reproducing the observed behavior of H₂ rovibration levels.

Instead, we compare the observed rovibration level distributions to thermal H₂ models. While thermal models alone will not explain the distributions and behaviors of H₂ in PPD sightlines, exploring various thermal distribution realizations will help place limits on the total thermal column density of H₂ in each PPD sightline.

We fit two thermal distributions to the rovibrational levels of each target:

1. Model 1: We fit purely thermal distributions of H₂ to all observed rovibrational states, regardless of excitation temperature.
2. Model 2: We fit purely thermal distributions of H₂ to only observed rovibrational states with $T_{exc} \leq 17,500$ K ($E'' \leq 1.5$ eV).

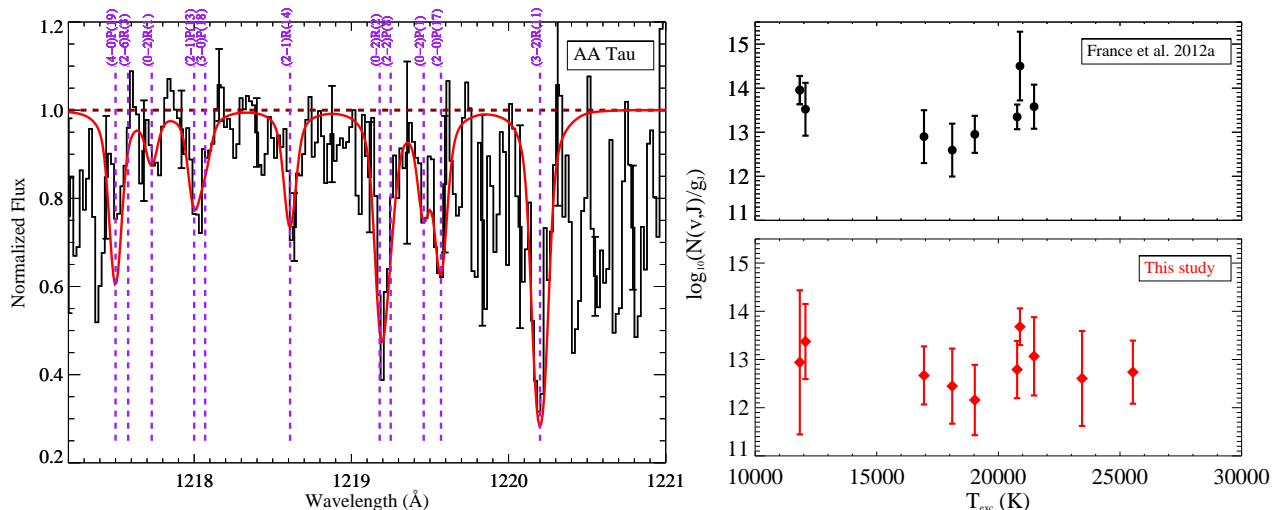


Figure 5. (a) *Left:* The best-fit synthetic H₂ absorption model (red) for AA Tau from 1217 – 1221 Å (black). Each transition is marked with dashed purple lines and identified with the progression ID. (b) *Right:* We compare our column density estimates, determined from the synthetic H₂ optical depth modeling framework (red, bottom), to results from France et al. (2012a) (black, top) in H₂ rotation diagrams. Both agree within the standard deviations determined from the absorption feature analysis and show comparable temperature slopes.

We discuss the details of the molecular physics and energy equations used for Models 1 and 2 in Appendix B. Each model is optimized to the rotation diagram of each target through a Markov Chain Monte Carlo (MCMC) routine, performed with the Python `emcee` package (Foreman-Mackey et al. 2013). The routine uses randomly-generated initial conditions and minimizes the likelihood function of the observed rovibrational column densities, given the range of model parameters. This process determines the best representative thermal model parameters ($N(\text{H}_2), T(\text{H}_2)$) to the data. Further details about the MCMC and parameter fits are discussed in Appendix C.

4.1. Thermal and Non-Thermal Column Densities

Each set of best-fit thermal model parameters is shown in Table 3. Figure 7 shows the rovibrational levels and thermal model realizations for RW Aur. We present data from this study (black circles) and lower excitation temperature states from France et al. (2014a) (black stars), which were detected against the FUV continuum between $\lambda\lambda$ 1092.5 – 1117 Å. RW Aur is the only target in our sample with both sets of H₂ data and provides an example for visualizing how higher excitation temperature ground states deviate from the warm thermal levels of H₂, which are likely probing the denser regions within the disk atmosphere ($\log_{10}(N(\text{H}_2)) = 19.90 \text{ cm}^{-2}$ and $T(\text{H}_2) = 440 \text{ K}$; magenta; France et al. 2014a). Higher energy rovibrational H₂ levels appear to scatter out of thermal equilibrium and are described by higher effective temperatures, as predicted by Nomura & Millar (2005). We present all H₂ rotation diagrams and thermal distribution realizations for each target in our survey in Appendix 4.

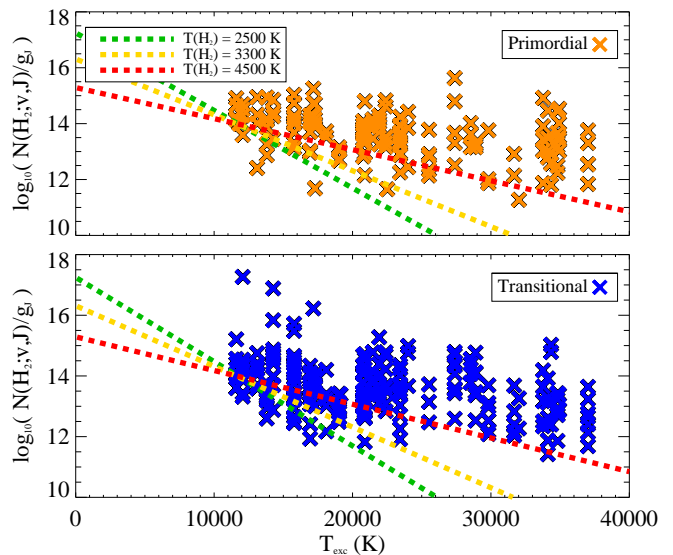


Figure 6. A relative comparison of H₂ rotation diagram behaviors. We normalize the rotation diagrams for H₂ distributions in all PPD sightlines to the $[v = 2, J = 1]$ level. We split these relative spectra by disk evolution, where primordial targets are shown at the top (orange) and transitional targets are shown at the bottom (blue). We fit thermally-distributed H₂ through the $[v = 2, J = 1]$ level for warm ($T(\text{H}_2) = 2500 \text{ K}$; green) and hot ($T(\text{H}_2) = 3500 \text{ K}$ and 4500 K ; yellow and red) H₂ populations.

Table 2 lists the average S/N of each Ly α emission profile as observed by either *HST*/COS or *HST*/STIS. We compute a Spearman rank coefficient between the best-fit thermal model $N(\text{H}_2)$ and the Ly α wing S/N and find

Table 2. Observed Ly α -Pumped H₂ Transitions

Blue Ly α Wing					Red Ly α Wing				
line ID ^a	λ_{pump}	f_{osc}^b	E''^c	A_{ul}	line ID ^a	λ_{pump}	f_{osc}^b	E''^c	A_{ul}
	(Å)	($\times 10^{-3}$)	(eV)	($\times 10^8 \text{ s}^{-1}$)		(Å)	($\times 10^{-3}$)	(eV)	($\times 10^8 \text{ s}^{-1}$)
B(1-2)R(5)	1210.352	36.3	1.19	1.4	C(1-5)R(5)	1216.988	7.1	2.46	0.39
C(0-3)R(19)	1210.449	25.4	2.94	1.1	C(1-5)R(9)	1216.997	19.7	2.76	0.80
B(1-2)P(4)	1210.631	29.1	1.13	1.7	B(3-3)R(2)	1217.031	1.24	1.50	0.04
C(2-5)P(11)	1210.682	30.1	2.91	1.5	B(3-3)P(1)	1217.038	1.28	1.48	0.17
C(1-4)R(17)	1211.048	37.2	3.00	1.6	B(0-2)R(0)	1217.205	44.0	1.00	0.66
C(1-5)P(3)	1211.402	7.5	2.36	0.48	C(0-4)Q(10)	1217.263	10.0	2.49	0.45
B(4-1)R(16)	1211.546	25.7	2.02	1.1	B(4-0)P(19)	1217.410	9.28	2.20	0.44
C(1-5)R(7)	1211.758	24.2	2.57	0.97	C(2-6)R(3)	1217.488	36.4	2.73	1.30
C(2-4)P(18)	1211.787	15.2	3.01	0.73	B(0-2)R(1)	1217.643	28.9	1.02	0.78
C(2-5)R(15)	1211.910	32.8	3.19	1.4	B(2-1)P(13)	1217.904	19.2	1.64	0.93
B(1-1)P(11)	1212.426	13.3	1.36	0.66	B(3-0)P(18)	1217.982	6.64	2.02	0.32
B(1-1)R(12)	1212.543	10.9	1.49	0.46	B(2-1)R(14)	1218.521	18.1	1.79	0.76
B(3-1)P(14)	1213.356	20.6	1.79	1.00	B(5-3)P(8)	1218.575	12.9	1.89	0.66
B(4-2)R(12)	1213.677	9.33	1.93	0.39	B(0-2)R(2)	1219.089	25.5	1.04	0.82
C(3-6)R(13)	1214.421	5.17	2.07	0.29	B(2-2)R(9)	1219.101	31.8	1.56	1.30
B(3-1)R(15)	1214.465	23.6	1.94	1.00	B(2-2)P(8)	1219.154	21.4	1.46	1.10
C(1-4)P(14)	1214.566	28.3	2.96	1.40	B(0-2)P(1)	1219.368	14.9	1.02	2.00
B(4-3)P(5)	1214.781	9.90	1.65	0.55	B(2-0)P(17)	1219.476	3.98	1.85	0.19
					B(0-1)R(11)	1219.745	3.68	1.36	0.15
					B(3-2)R(11)	1220.110	21.3	1.80	0.88
					B(0-1)P(10)	1220.184	5.24	1.23	0.26

^a Describes ground state-to-excited state transition, due to absorption of Ly α photon λ_{pump} . IDs beginning with “B” are excited to Lyman excitation level ($2p\sigma B^1\Sigma_u^+$), and IDs beginning with “C” are excited to Werner excitation state ($2p\pi C^1\Pi_u$).

^b The oscillator strength of the transition.

^c The energy level of ground state ($X^1\Sigma_g^+$) H₂ before photo-excitation.

significant trends for both Model 1 ($\rho = -0.71$, with a probability to exceed the null hypothesis that the data are drawn from random distributions ($p^1 = 7.0 \times 10^{-3}$) and Models 2 ($\rho = -0.78$, $p = 5.6 \times 10^{-2}$). However, when we exclude one low S/N data point from the correlation (LkCa 15) and re-calculate the Spearman rank coefficient for both model realizations, we see a more randomly-distributed set of modeled column density estimates (Model 1: $\rho = -0.22$, $p = 3.91 \times 10^{-1}$ and Model 2: $\rho = -0.27$, $p = 1.92 \times 10^{-1}$). Therefore, for the remainder of this study, we do not include LkCa 15 results in further analysis.

¹ The strength of p is defined as follows: $p > 5\%$ (5.0×10^{-2}) = no correlation; $1\% < p < 5\%$ = possible correlation; $0.1\% < p < 1\%$ = correlation; $p < 0.1\%$ = strong correlation.

We use the results from Models 1 and 2 to estimate the total column density of thermally-distributed H₂ ($N(\text{H}_2)$) in each sight line. We choose to represent the thermal distributions of hot H₂ with the results from Model 2. $T(\text{H}_2)$ from Model 2 represents a more realistic determination of the bulk temperature profiles of thermal H₂ ($T(\text{H}_2) \sim 2500 - 3500$ K) in each sight-line, whereas Model 1 produces $T(\text{H}_2) \approx T_{diss}(\text{H}_2)$. In reality, there is very little difference between $N(\text{H}_2)$ determined from Models 1 and 2; both model realizations predict similar $N(\text{H}_2)$, though Model 2 results tend to under-predict $N(\text{H}_2)$ when compared to Model 1 results, and thus provide a lower limit to the total thermal column density of hot H₂.

To approximate how much of the total observed H₂ column density is associated with excess H₂ populations in highly energetic (non-thermal) states, we define a metric for the total non-thermal column density of H₂

Table 3. Thermal H₂ Column Density & Temperature Results

Target	v_r^*	Model 1		Model 2		N(H ₂) _{nLTE} ^a	N(H ₂ [5,18]) ^{a,c}
		N(H ₂) ^a	T(H ₂) ^b	N(H ₂) ^a	T(H ₂) ^b		
AA Tau	20.1	16.27 ^{+0.50} _{-0.34}	4179 ⁺⁵⁸⁵ ₋₈₈₇	15.85 ^{+0.11} _{-0.11}	3578 ⁺²⁸² ₋₂₂₁	16.40 ^{+0.01} _{-0.01}	10.35
AB Aur	-12.8	15.59 ^{+0.31} _{-0.20}	4488 ⁺³⁷⁶ ₋₇₀₄	15.34 ^{+0.34} _{-0.26}	3628 ⁺⁷⁴⁴ ₋₆₃₁	15.44 ^{+0.01} _{-0.01}	-
AK Sco	-4.3	15.57 ^{+0.17} _{-0.16}	4880 ⁺⁹⁰ ₋₁₉₀	15.52 ^{+0.51} _{-0.29}	3661 ⁺⁸⁷² ₋₉₂₂	15.04 ^{+0.05} _{-0.01}	-
BP Tau	22.4	15.50 ^{+0.21} _{-0.19}	4855 ⁺¹⁰⁷ ₋₂₂₀	15.11 ^{+0.55} _{-0.31}	3693 ⁺⁸⁶⁸ ₋₉₇₂	15.37 ^{+0.01} _{-0.02}	10.72
CS Cha	13.6	15.82 ^{+0.17} _{-0.16}	4889 ⁺⁸³ ₋₁₇₄	15.27 ^{+0.57} _{-0.34}	3536 ⁺⁹⁵⁴ ₋₉₆₂	15.52 ^{+0.01} _{-0.02}	9.92
DE Tau	11.8	16.20 ^{+0.50} _{-0.32}	4082 ⁺⁶⁴⁴ ₋₉₂₇	16.08 ^{+0.86} _{-0.50}	3466 ⁺¹⁰³⁰ ₋₁₁₂₀	16.03 ^{+0.01} _{-0.01}	-
DF Tau A	34.8	15.13 ^{+0.29} _{-0.19}	4375 ⁺⁴⁴³ ₋₆₉₅	14.98 ^{+0.09} _{-0.09}	3382 ⁺¹⁸⁸ ₋₁₅₉	14.74 ^{+0.01} _{-0.01}	11.19
DM Tau	40.6	16.02 ^{+0.20} _{-0.18}	4810 ⁺¹⁴⁰ ₋₂₇₄	16.14 ^{+0.75} _{-0.54}	2900 ⁺¹¹⁷⁰ ₋₇₇₆	15.90 ^{+0.01} _{-0.02}	10.23
GM Aur	25.4	15.84 ^{+0.18} _{-0.17}	4873 ⁺⁹⁵ ₋₂₀₀	15.67 ^{+0.68} _{-0.50}	2966 ⁺¹⁰⁹⁶ ₋₇₆₂	15.51 ^{+0.01} _{-0.02}	-
HD 104237	0.6	15.95 ^{+0.27} _{-0.26}	4831 ⁺¹²⁶ ₋₂₆₄	15.16 ^{+0.46} _{-0.28}	3734 ⁺⁸³⁰ ₋₉₀₆	16.47 ^{+0.01} _{-0.01}	-
HD 135344 B	6.7	15.60 ^{+0.18} _{-0.17}	4886 ⁺⁸⁶ ₋₁₈₁	15.24 ^{+0.42} _{-0.29}	3544 ⁺⁸⁷⁸ ₋₇₇₀	15.26 ^{+0.01} _{-0.02}	-
HN Tau A	24.2	16.92 ^{+1.03} _{-0.64}	3035 ⁺¹¹⁹³ ₋₉₆₆	16.85 ^{+1.08} _{-0.72}	2798 ⁺¹³⁰⁵ ₋₉₁₂	14.63 ^{+1.20} _{-0.20}	-
LkCa15	35.0	17.77 ^{+0.62} _{-0.51}	4556 ⁺³²⁴ ₋₆₁₁	17.35 ^{+0.11} _{-0.11}	3516 ⁺²⁶⁰ ₋₂₀₀	17.64 ^{+1.50} _{-0.20}	10.01
RECX 11	24.5	15.84 ^{+0.13} _{-0.13}	4905 ⁺⁷¹ ₋₁₄₇	15.55 ^{+0.24} _{-0.17}	3939 ⁺⁶²⁹ ₋₆₁₁	15.64 ^{+0.01} _{-0.01}	9.98
RECX 15	-2.7	16.03 ^{+0.21} _{-0.20}	4858 ⁺¹⁰⁶ ₋₂₁₉	15.47 ^{+0.47} _{-0.27}	3944 ⁺⁷²⁹ ₋₉₅₀	15.63 ^{+0.01} _{-0.02}	9.48
RU Lupi	6.8	16.03 ^{+0.21} _{-0.19}	4765 ⁺¹⁷⁴ ₋₃₃₆	15.38 ^{+0.61} _{-0.34}	3840 ⁺⁸⁰⁷ ₋₁₁₀₆	15.66 ^{+0.01} _{-0.02}	-
RW Aur A	12.4	16.23 ^{+0.29} _{-0.27}	4822 ⁺¹³³ ₋₂₆₃	15.60 ^{+0.56} _{-0.33}	3729 ⁺⁸⁵⁸ ₋₁₀₀₅	17.36 ^{+0.01} _{-0.01}	-
SU Aur	36.0	16.21 ^{+0.51} _{-0.38}	4264 ⁺⁵²⁵ ₋₈₀₂	16.51 ^{+3.48} _{-1.22}	2574 ⁺¹⁶⁵⁴ ₋₁₅₆₅	15.31 ^{+3.00} _{-0.20}	-
SZ 102	-20.7	15.43 ^{+0.20} _{-0.15}	4493 ⁺³⁶² ₋₅₃₀	15.83 ^{+0.32} _{-0.34}	2785 ⁺⁵⁸⁸ ₋₃₆₆	15.26 ^{+0.01} _{-0.01}	-
TW Hya	19.6	15.40 ^{+0.17} _{-0.16}	4880 ⁺⁸⁹ ₋₁₉₂	15.08 ^{+0.54} _{-0.33}	3483 ⁺⁹⁵⁴ ₋₈₈₇	15.19 ^{+0.01} _{-0.02}	11.31
UX Tau A	33.0	16.76 ^{+0.38} _{-0.34}	4668 ⁺²⁴⁴ ₋₄₆₀	16.40 ^{+1.32} _{-0.56}	3129 ⁺¹²⁸³ ₋₁₃₈₃	16.38 ^{+2.60} _{-0.20}	-
V4046 Sgr	-4.7	15.33 ^{+0.15} _{-0.14}	4894 ⁺⁸⁰ ₋₁₆₄	15.05 ^{+0.40} _{-0.25}	3900 ⁺⁷⁴⁰ ₋₈₉₁	15.05 ^{+0.01} _{-0.01}	10.27
Avg. Model Results		15.97 ^{+1.80} _{-0.84}	4604 ⁺³⁰¹ ₋₁₅₇₀	15.70 ^{+1.65} _{-0.72}	3442 ⁺⁵⁰⁰ ₋₈₇₀		

*The radial velocity of the system, derived from the synthetic H₂ optical depth curves, are expressed as km s⁻¹.

^aAll column densities are to the power of 10 (log₁₀N(H₂)).

^bThermal temperatures of the bulk H₂ populations (T(H₂)) are in Kelvin.

^cEstimated from the formalism outlined in Rosenthal et al. (2000) (Equation 1). We assume the H₂[5,18] population is optically thin.

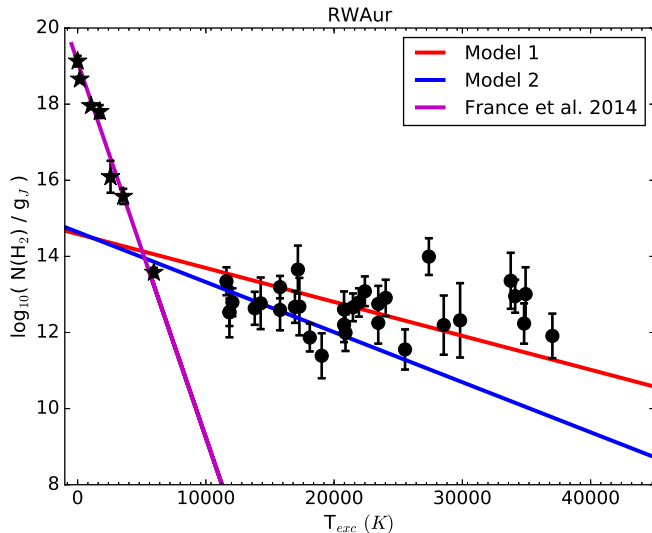


Figure 7. The rotation diagram for RW Aur, with rovibrational column densities derived in this study (black circles) and lower energy states measured by France et al. (2014a) (black stars; $\lambda\lambda$ 1092.5 – 1117 Å). The red and blue solid lines represent thermal distributions of H₂ levels populated in Models 1 and 2, respectively. The magenta solid line shows the thermal distribution H₂ levels examined by France et al. (2014a), with $\log_{10}(N(\text{H}_2)) = 19.90 \text{ cm}^{-2}$ and $T(\text{H}_2) = 440 \text{ K}$.

in highly excited levels ($E'' > 1.75 \text{ eV}$, or $T_{exc} > 20,000 \text{ K}$), which we refer to as $N(\text{H}_2)_{\text{nLTE}}$. $N(\text{H}_2)_{\text{nLTE}}$ is calculated by integrating the residual between observed H₂ rovibration levels with $T_{exc} > 20,000 \text{ K}$ and the predicted populations of H₂ at that same rovibration level from the modeled thermal distributions, or $N(\text{H}_2)_{\text{nLTE}} = \sum_{[v,J]} (N(\text{H}_2[v,J])_{\text{obs}} - N(\text{H}_2[v,J])_{\text{model}})$. For consistency, we calculate $N(\text{H}_2)_{\text{nLTE}}$ from all best-fit model realizations from both Models 1 and 2. We find we are able to produce approximately the same $N(\text{H}_2)_{\text{nLTE}}$ estimate from $N(\text{H}_2)$ of both Models 1 and 2. Associated error bars on $N(\text{H}_2)_{\text{nLTE}}$ are estimated as the minimum and maximum deviations away from the median $N(\text{H}_2)_{\text{nLTE}}$ for all Model 1 and Model 2 best-fit thermal parameters. Table 3 includes our estimates of $N(\text{H}_2)_{\text{nLTE}}$ for each target (for which we include LkCa 15, but we do not use in further analysis).

4.2. C IV-Pumped H₂ Fluorescence

Molecular hydrogen populations photo-excited by C IV photons (λ 1548.20, 1550.77 Å) are found in highly excited ground states ([3,25], [5,18], and [7,13]; $E'' \geq 3.8 \text{ eV}$, $T_{exc} > 43,000 \text{ K}$) that are difficult to explain with thermally-generated H₂ populations alone. These highly excited states are also unlikely to be directly populated by the fluorescence process. Electronic transitions are dipole-allowed, meaning $J' - J'' = \pm 1$ or 0 (for Werner band lines with $J'' \neq 0$) between excited and ground state transitions. The decay from excited electronic to

ground states can easily increase the ground electronic vibrational levels, but will not substantially change the ground electronic quantum rotational levels (Herczeg et al. 2006). Therefore, other physical mechanisms, such as collisional (Bergin et al. 2004) and chemical (Takahashi et al. 1999; Ádámkóvics et al. 2016) processes, must be responsible for populating these highly energetic levels of H₂.

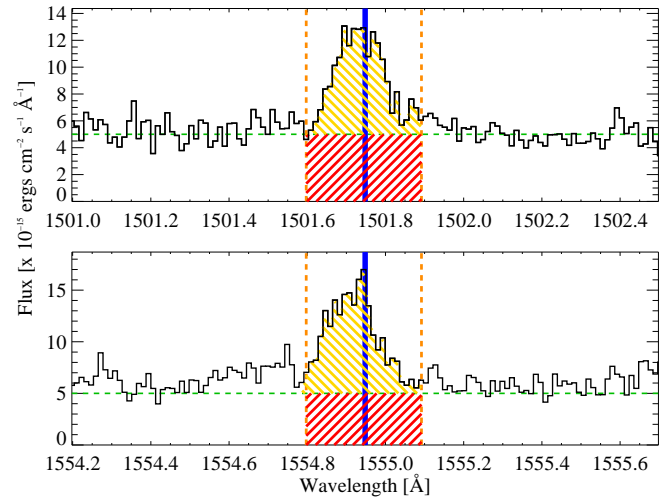


Figure 8. The presence of C IV-pumped H₂ emission from the B(0-5)P(18) progression. We present example fluorescence lines for BP Tau, for emission lines at 1501.75 Å ((0-5)R(16)) and 1554.95 Å ((0-6)R(16)), indicated by the blue dotted lines. The green dashed line shows the continuum levels in each spectral region. The orange dashed lines mark off the region considered for each fluorescence line. The yellow hashed region represents the integrated flux $F(\text{C IV-H}_2)$ within the orange region, while the red hashed region represents the integrated continuum flux in the same region.

Since we do not know which processes dominate the pumping of H₂ into these highly energetic upper rotational levels, we use the emission from C IV-pumped H₂ as a proxy for a variety of non-thermal processes that may excite H₂ to highly non-thermal states. We estimate the column density of H₂ populating these energetic levels from the total fluorescent emission produced by C IV-pumped H₂. We stipulate two conditions to verify whether the target exhibits C IV-pumped H₂ emission in the FUV spectrum: 1) each emission line must have an elevated flux level $\geq 1.5\sigma$ above the continuum floor, and 2) at least two emission lines from the same progression must be present. Figure 8 demonstrates how we determine that the emission line exists above the FUV continuum. Only fluorescence from the B(0-5)P(18) 1548.15 Å transition meets this criteria for targets which show signs of C IV-pumped H₂ emission in our survey. The two brightest transitions from the B(0-5)P(18) 1548.15 Å cascade, λ 1501.75 Å and λ 1554.95

Å, are free of blending from other atomic or molecular contaminants (Herczeg et al. 2006). Therefore, emission features observed at these wavelengths are detected fluorescence transitions, originating from the highly non-thermal H₂ state [5,18]. Of the 22 targets, 10 show statistically significant emission lines from C IV-pumped H₂ fluorescence.

To estimate the density of highly excited H₂, we use the flux from the two brightest emission features at λ 1501.75 Å and λ 1554.95 Å, after subtracting the UV continuum. We assume that H₂[5,18] is optically thin and estimate the total column density of this highly non-thermal ground state (N(C IV-H₂)) from the formalism described in Rosenthal et al. (2000),

$$N(\text{CIV} \rightarrow \text{H}_2[v'', J'']) = \frac{4\pi\lambda}{hc} \frac{F(\text{CIV-H}_2)([v', J'] \rightarrow [v'', J''])}{A_{ul}([v', J'] \rightarrow [v'', J''])} \quad (1)$$

where N(C IV→H₂[v'', J'']) is the column density of C IV-pumped H₂ that decays to ground state [v'', J''], λ is the transition wavelength between electronic and ground states, F(C IV-H₂) is the integrated flux in the emission line produced by the transition between excited electronic level [v', J'] and ground level [v'', J''], and A_{ul} is the spontaneous decay rate for the transition. For each emission line, we calculate N(C IV-H₂) and take the average of the results from the two emission features as the estimate of N(C IV-H₂). Error bars on N(C IV-H₂) are taken as the residual between the N(C IV-H₂) and the column density derived from each emission feature at λ 1501.75 Å and λ 1554.95 Å. Derived N(C IV-H₂) values are listed in Table 3. All column densities derived from the fluorescence emission from the B(0-5)P(18) progression are $\log_{10}(\text{N}(\text{C IV-H}_2)) < 12.0 \text{ cm}^{-2}$, which is consistent with a thin layer of highly energetic H₂ (Herczeg et al. 2006).

5. DISCUSSION

This study has focused on characterizing the column density of H₂ from observed distributions of rovibrational states derived from their respective absorption features embedded within the stellar Ly α wings of PPD hosts. We discovered that we systematically find higher excitation levels with larger column densities than expected from thermally-distributed, warm populations of H₂. The observed H₂ distributions of rovibrational states tells us that some mechanism or mechanisms in and/or around the circumstellar environment is/are affecting the equilibrium state of warm molecules in these sightlines. We aim to characterize the general behavior of thermal and non-thermal H₂ populations and column densities in PPD environments by comparing these quantities to stellar and circumstellar observables.

First, we look for correlations between the modeled distributions of warm, thermal H₂ (T(H₂) > 2500 K) and the populations of non-thermal H₂ states for the sampled PPD sightlines. Figure 9 compares thermal, model-derived N(H₂) to the sum of the residuals in

highly-energetic H₂ states, N(H₂)_{nLTE}. Before noting the distributions of total column densities by categorization, we see that the general trend between the distributions of N(H₂) and N(H₂)_{nLTE} appear roughly related, with a Spearman rank coefficient which agrees with this assessment ($\rho = +0.54$), but a PTE that suggests there is no strong indication of a trend between the two variables ($p = 1.17 \times 10^{-1}$). However, when we categorize targets by their disk evolution and whether C IV-pumped H₂ fluorescence is detected in their FUV spectra, we see much clearer trends that point to target distributions which have correlated N(H₂) and N(H₂)_{nLTE} populations. Transitional disks appear to predominantly straddle the N(H₂) = N(H₂)_{nLTE} equality line ($\rho = +0.62$, $p = 2.00 \times 10^{-2}$), and targets which have detectable C IV-pumped H₂ fluorescence show the same behavior ($\rho = +0.83$, $p = 6.03 \times 10^{-3}$). Primordial disk targets appear to have more scattered distributions of N(H₂) and N(H₂)_{nLTE} ($\rho = +0.31$, $p = 5.69 \times 10^{-1}$), as do targets with no detected C IV-pumped H₂ fluorescence ($\rho = +0.24$, $p = 4.82 \times 10^{-1}$).

5.1. H₂ Column Densities & the Circumstellar Environment

We first consider the role of excess FUV and X-ray emission on the modeled thermal and non-thermal total column densities of H₂, to explore if the distributions of observed H₂ levels match the behaviors observed in Nomura & Millar (2005) and Nomura et al. (2007). We split the various excess emission into the following categories: the total X-ray luminosity (L_X; France et al. 2017 and references therein), the total FUV continuum luminosity (L_{FUV}: $\lambda\lambda$ 1490 – 1690 Å, excluding any discrete or extended emission features; France et al. 2014b), the total H₂ dissociation continuum around λ 1600 Å (L_{Bump}; France et al. 2017), and the total observed flux, corrected for ISM reddening, of FUV continuum+discrete emission features from $\lambda\lambda$ 912 – 1150 Å (F_{1110Å}; France et al. 2014b). Figure 10 shows the comparison of N(H₂) and N(H₂)_{nLTE} to these circumstellar observables. We note a correlation between L_X and N(H₂)_{nLTE} ($\rho = +0.53$, $p = 4.00 \times 10^{-2}$), but no correlation between N(H₂) and L_X ($\rho = +0.15$, $p = 6.62 \times 10^{-1}$). We observe an anti-correlation between N(H₂)_{nLTE} and L_{Bump} ($\rho = -0.62$, $p = 1.90 \times 10^{-2}$) and no strong trend between N(H₂) and L_{Bump} ($\rho = -0.16$, $p = 5.83 \times 10^{-1}$). We again find an anti-correlation between N(H₂)_{nLTE} and F_{1110Å} ($\rho = -0.54$, $p = 4.81 \times 10^{-2}$), yet no indication of a trend between N(H₂) and F_{1110Å} ($\rho = -0.21$, $p = 5.14 \times 10^{-1}$). Finally, both N(H₂) and N(H₂)_{nLTE} show suggestive anti-correlations with L_{FUV}, but they are not statistically significant (N(H₂): $\rho = -0.42$, $p = 1.02 \times 10^{-1}$; N(H₂)_{nLTE}: $\rho = -0.48$, $p = 7.30 \times 10^{-2}$).

Next, we look at how discrete emission line features (from the protostar and accretion shock regions) and disk fluorescence processes may play a role on the total column densities of H₂ in PPD sightlines. We split the

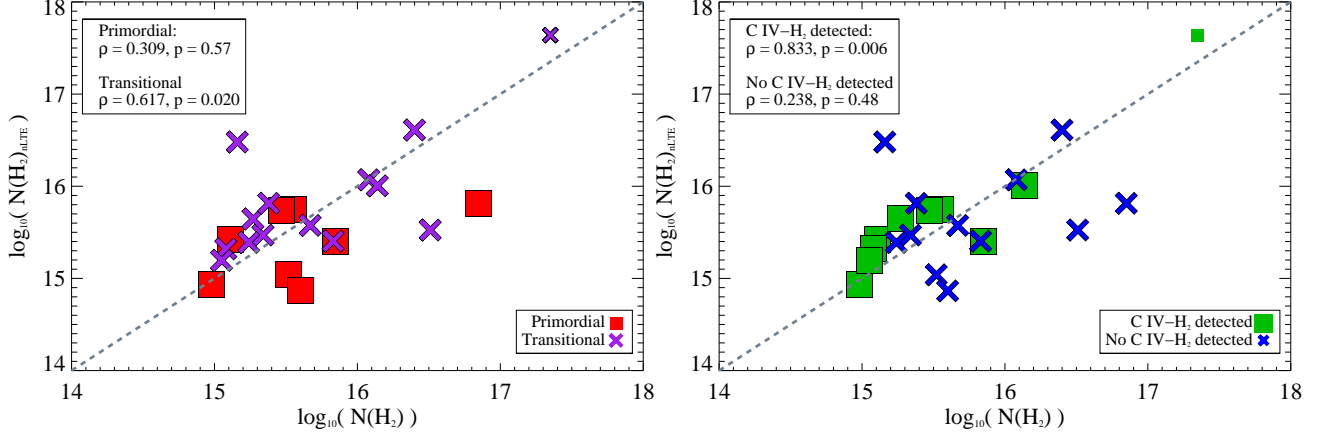


Figure 9. We compare model-derived $N(\text{H}_2)$ to $N(\text{H}_2)_{\text{nLTE}}$ and separate populations by disk evolutionary phase (*left*) and whether there is evidence of C IV-pumped H_2 fluorescence in the FUV spectrum (*right*). Transitional disk targets and targets with detected C IV-pumped H_2 fluorescence (AA Tau, BP Tau, CS Cha, DF Tau, DM Tau, LkCa 15, RECX 11, RECX 15, TW Hya, and V4046 Sgr) appear to have direct correlations with $N(\text{H}_2) \sim N(\text{H}_2)_{\text{nLTE}}$.

circumstellar parameters into the following categories: the total luminosity from stellar+shock-generated Ly α emission ($L_{\text{Ly}\alpha}$; ; France et al. 2014b), the total luminosity from stellar+shock-generated C IV emission (L_{CIV} ; France et al. 2014b), the total H_2 fluorescence luminosity from Ly α -pumped H_2 predominantly produced in the disk atmosphere (L_{H_2} ; France et al. 2014b), and the estimated total column density of $\text{H}_2[5,18]$, derived from the statistically-determined C IV-pumped fluorescence features ($N(\text{C IV-H}_2)$, derived in Section 4.2). Figure 11 shows the comparison of $N(\text{H}_2)$ and $N(\text{H}_2)_{\text{nLTE}}$ to these circumstellar variables. We find no trends between the modeled column densities of H_2 and $L_{\text{Ly}\alpha}$ ($N(\text{H}_2)$: $\rho = -0.31$, $p = 2.34 \times 10^{-1}$; $N(\text{H}_2)_{\text{nLTE}}$: $\rho = -0.04$, $p = 7.86 \times 10^{-1}$), as well as L_{H_2} ($N(\text{H}_2)$: $\rho = -0.25$, $p = 3.45 \times 10^{-1}$; $N(\text{H}_2)_{\text{nLTE}}$: $\rho = -0.06$, $p = 7.54 \times 10^{-1}$). We do see a suggestive anti-correlation between L_{CIV} and $N(\text{H}_2)$ ($\rho = -0.51$, $p = 4.52 \times 10^{-2}$), but no trend between $N(\text{H}_2)_{\text{nLTE}}$ and L_{CIV} ($\rho = -0.19$, $p = 5.62 \times 10^{-1}$). Finally, we find anti-correlated behavior between both $N(\text{H}_2)$ and $N(\text{H}_2)_{\text{nLTE}}$ with $N(\text{C IV-H}_2)$ ($N(\text{H}_2)$: $\rho = -0.51$, $p = 1.71 \times 10^{-2}$; $N(\text{H}_2)_{\text{nLTE}}$: $\rho = -0.43$, $p = 5.50 \times 10^{-2}$).

5.2. The Behavior of Hot H_2

We find that the column densities of H_2 are correlated to many non-thermal diagnostics of the circumstellar environment, such as internal radiation and H_2 dissociation tracers. Therefore, the observed distribution of H_2 absorption populations appear to be located somewhere in the disk environment where 1) 1) the H_2 have access to protostellar radiation with $\lambda < 1110 \text{ \AA}$, and 2) the H_2 populations are optically-thin to Ly α radiation. Piecing our results together, we suspect that the observed H_2 populations against the protostellar Ly α wing provide are not associated with the H_2 that fluoresces in the disk and may, instead, arise from a hot,

tenuous disk halo. Ádámkóvics et al. (2016) explore the effects of FUV, X-ray, and Ly α radiation on stratified layers of molecular PPD atmospheres. In the presence of all three, FUV continuum and X-ray radiation create a hot, atomic layer along the uppermost disk surface, and Ly α radiation penetrates deeper into the disk via H I scattering. The penetration of Ly α into the molecular disk is found to photodissociate trace molecules like H_2O and OH, which, along with H_2 formation on dust grains, heat this region of the disk and create a warm molecular layer ($T_{\text{gas}} > 1500 \text{ K}$). This warm layer is found to have an appreciable column of warm H_2 ($N(\text{H}_2) > 10^{19} \text{ cm}^{-2}$) in the appropriate temperature regime to reproduce fluorescent emission signatures in PPDs, though the distribution of H_2 rovibrational levels is not computed in the Ádámkóvics et al. (2016) models.

The Ádámkóvics et al. (2016) study produces a hot ($T \sim 5000 \text{ K}$) atomic layer in the uppermost disk atmosphere, which is similar in nature to a photodissociation region (PDR; Hollenbach & Tielens 1999 and references therein). This hot atomic layer is produced in all of their model parameter space, independent of stellar Ly α luminosity or dust grain distributions. This layer of hot atomic gas contains a minute abundance of H_2 ($x(\text{H}_2) \lesssim 10^{-5}$) with total column densities of hot H_2 similar to those found in this study ($N(\text{H}_2)_{\text{hotlayer}} \sim 10^{15} \text{ cm}^{-2}$; $\langle N(\text{H}_2)_{\text{H}_2\text{abs}} \rangle \sim 10^{15.5} \text{ cm}^{-2}$). This hot atomic layer is modeled above the warm molecular layer (where H_2 fluorescence may arise) and extends substantially further away from the disk midplane (Ádámkóvics et al. 2016). What their study finds is that Ly α radiation is key to producing the warm molecular regions that may be associated with warm H_2 and CO populations, but the hot, atomic layer is driven by the FUV continuum and X-ray luminosities, which cannot penetrate into the cooler disk like Ly α can.

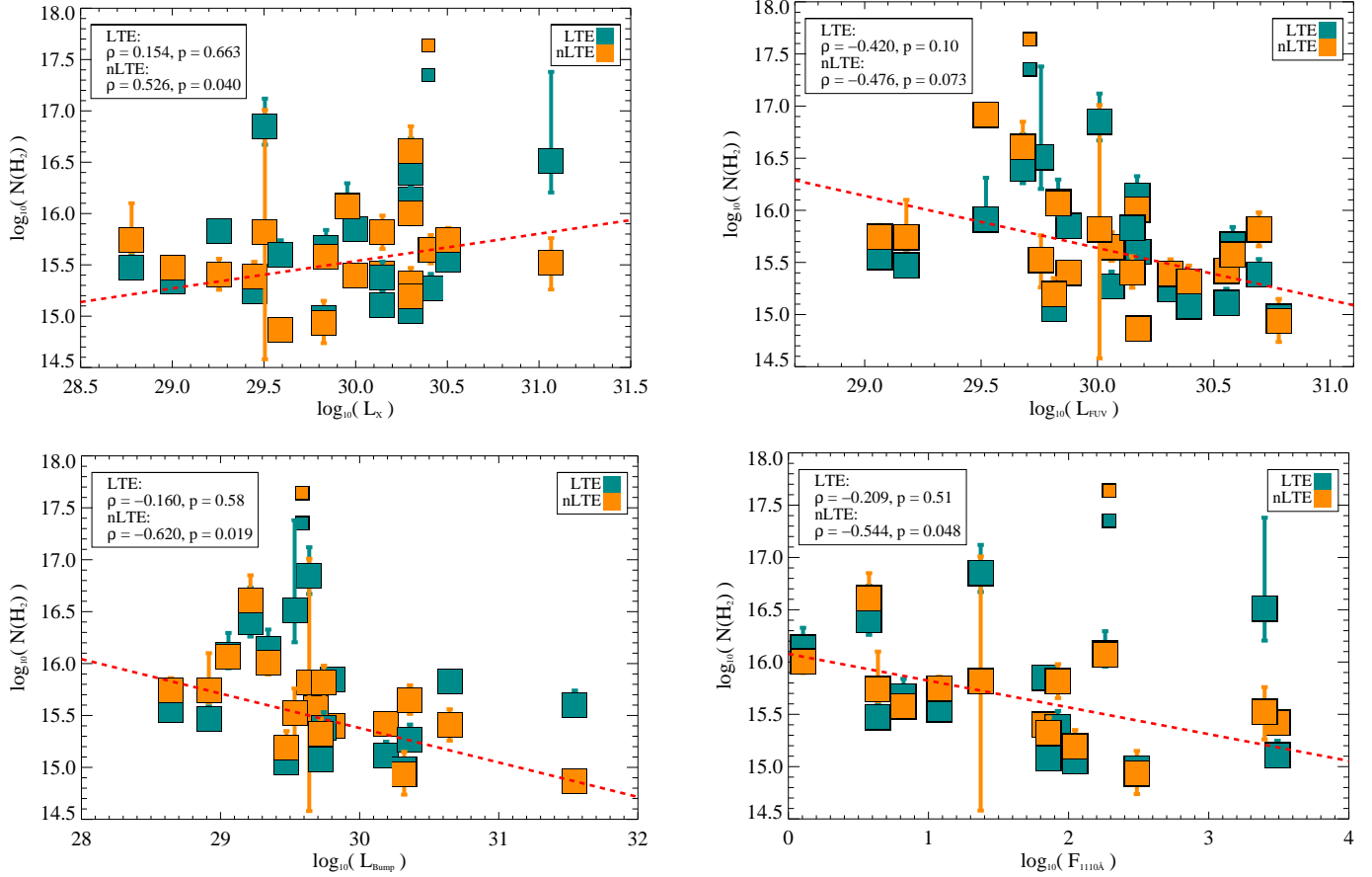


Figure 10. We compare the total column densities of thermal and non-thermal H₂ to the total X-ray luminosity (*top left*), the total FUV continuum luminosity (*top right*), the total H₂ dissociation “bump” luminosity around λ 1600 Å (*bottom left*), and the integrated flux from λ 912 – 1150 Å estimated at 1 AU from each protostar (*bottom right*). $N(\text{H}_2)$ shows no significant correlations with any high-energy radiation observables, while $N(\text{H}_2)_{\text{nLTE}}$ shows confident trends with L_X , L_{Bump} , and $F_{1110\text{\AA}}$. Both total column densities show a very loose trend with L_{FUV} . LkCa 15 is included in each plot as smaller square symbols. Outside of log space, the column density variables have units of cm^{-2} , the luminosity variables have units of erg s^{-1} , and the flux variables have units of $\text{erg cm}^{-2} \text{s}^{-1}$.

Connecting the findings from this work and the [Ádámkóvics et al. \(2016\)](#) models, we suggest that the observed H₂ absorption populations, probed in the wings of protostellar Ly α profiles, reside in this tenuous, hot atomic region of the circumstellar environment. We argue that the behavior of the Ly α transition, being by nature a powerful resonance line, allows Ly α radiation to scatter through both the PPD and the surrounding PDR-like environment. Rather than probing a discrete line source coming straight from the accretion shock near the protostellar surface, we probe Ly α that has scattered through the circumstellar environment by H I atoms before reaching the observer. The scattering of Ly α radiation by H I, which occurs when a Ly α photon is absorbed and emitted many times into many different directions and results in changes in the frequency of Ly α away from rest wavelength, causes significant broadening of the Ly α profile on order of several hundred km s^{-1} before escaping the star (see [McJunkin et al. 2014](#) for

a more complete overview of this process). It appears that the H₂ probed in absorption against these observed Ly α wings may be tied to this optically-thin, hot halo surrounding the PPD, where optically-thin densities of H₂ absorb Ly α before it can exit the system. Figure 12 presents a cartoon disk showing the possible locations of H₂ fluorescence populations (blue), warm H₂ in the disk (red), and the hot halo of gas where H₂ is probed against the protostellar Ly α profile (diffuse red haze). For now, this haze is assumed to be anywhere surrounding the protostar and protoplanetary disk. Additional work is being conducted to constrain the spatial origins of these hot H₂ populations.

5.2.1. H₂ “Multiple Pumping” Versus Cooling

The scattering of Ly α radiation through the hot atomic regions surrounding PPDs may help explain the non-thermal behavior of H₂ associated with these environments. The behavior of the observed rovibra-

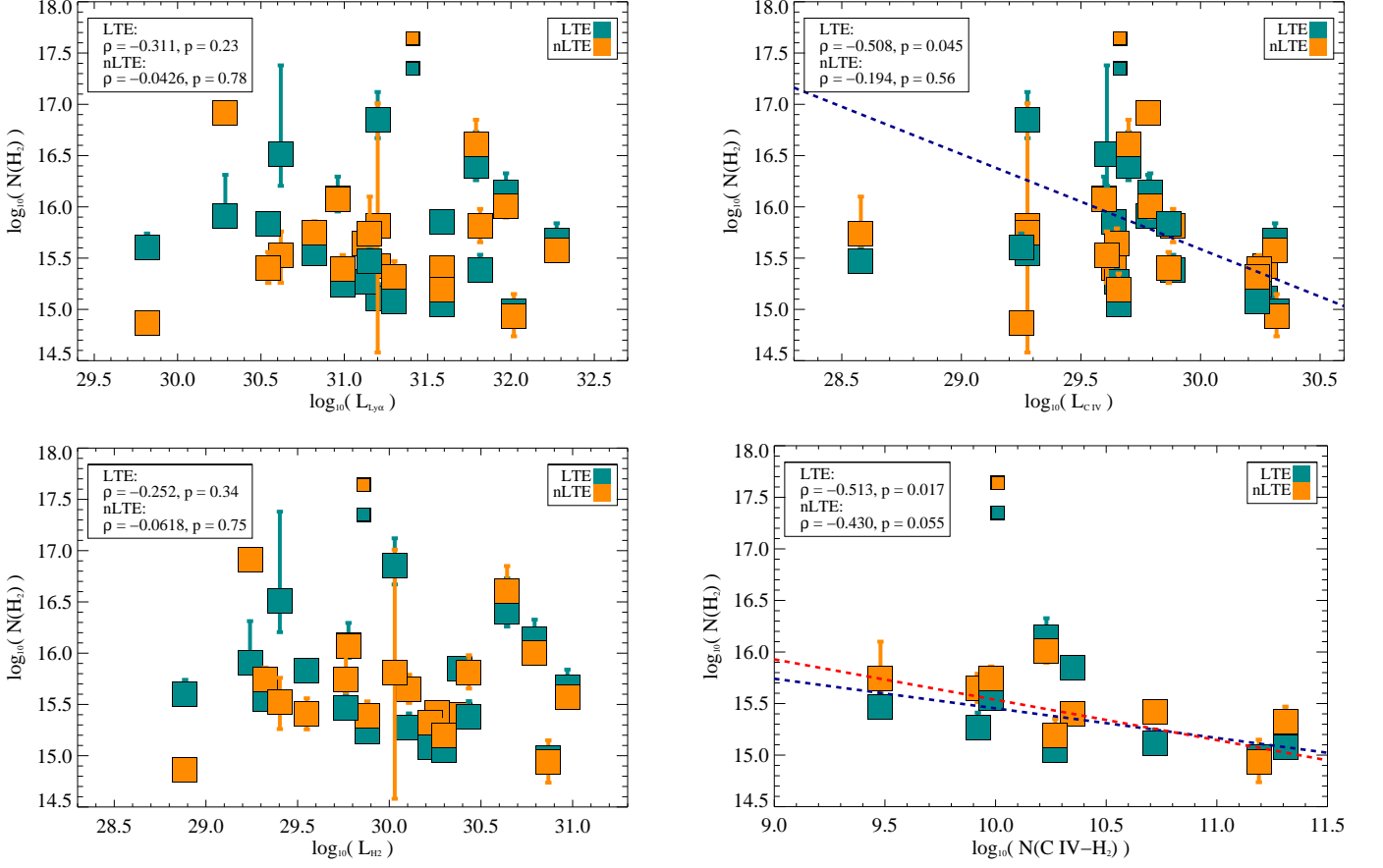


Figure 11. We compare the total column densities of thermal and non-thermal H₂ to the total Ly α luminosity (*top left*), the total C IV luminosity (*top right*), the total H₂ fluorescence luminosity (*bottom left*), and the total column density of H₂ found in H₂[5,18] (*bottom right*). $N(\text{H}_2)$ shows confident trends with L_{CIV} and $N(\text{C IV-H}_2)$, while $N(\text{H}_2)_{\text{nLTE}}$ only displays a loose trend with $N(\text{C IV-H}_2)$. We find no correlations between the modeled H₂ column densities and $L_{\text{Ly}\alpha}$ and L_{H_2} . LkCa 15 is included in each plot as smaller square symbols. Outside of log space, the column density variables have units of cm^{-2} and the luminosity variables have units of erg s^{-1} .

tional levels may be the result of “multiple pumping” happening with the hot H₂, meaning that the excitation rate by UV photon absorption (in this case, specifically Ly α photons) is faster than the molecules can decay (cool) via rovibrational emission lines or collisions.

We perform a back-of-the-envelope comparison of the H₂ rovibrational emission and total collision rates required to balance H₂ photo-excitation (“Ly α -pumping”), assuming the H₂ species are located in a hot atomic layer above the PPD. The hot atomic region is assumed to be a plane-parallel slab above the inner disk ($r < 1$ AU; [Ádámkóvics et al. 2016](#)) with a thickness $a \sim 1$ AU. We assume the average Ly α luminosity for a typical PPD system $\langle L_{\text{Ly}\alpha} \rangle \sim 10^{31}$ erg s^{-1} ([Schindhelm et al. 2012](#); [France et al. 2014b](#)), which translates into an average photon rate $\langle \Gamma_{\text{Ly}\alpha} \rangle = \langle L_{\text{Ly}\alpha} \rangle / E_{\text{Ly}\alpha} \sim 10^{42}$ photons s^{-1} incident on the hot H₂. Since H₂ is expected to only be a trace species in this region ($x(\text{H}_2) \sim 10^{-5}$; [Ádámkóvics et al. 2016](#)), we include a “coverage factor” for the total Ly α luminosity on the

H₂ populations. This leads to an estimation of the total photo-excitation rate of H₂ in the hot atomic layer, $\langle \Gamma_{\text{Ly}\alpha} \rangle \sim x(\text{H}_2) \times 10^{42}$ $\text{photons s}^{-1} \sim 10^{37}$ photons s^{-1} . We calculate the average rate of incident Ly α photons on the H₂ populations in the PDR slab to be $\gamma_{\text{Ly}\alpha} \sim \langle \Gamma_{\text{Ly}\alpha} \rangle / (\sigma(\text{H}_2) \times a^2) \approx 10^{-3}$ photon s^{-1} , where $\sigma(\text{H}_2)$ is the average Ly α line absorption cross-section of an individual molecules, given by

$$\sigma(\text{H}_2) = \frac{\sqrt{\pi} e^2}{m_e c b_{\text{H}_2}} \lambda_i f_i \quad (2)$$

([McCandliss 2003](#); [Cartwright & Drapatz 1970](#)), where λ_i is the absorption wavelength for a given transition in the Ly α profile (taken as 1215.67 Å for this example), f_i is the oscillator strength (the average assumed as ≈ 0.01), and b_{H_2} is the b-value of the line, assumed to match our models ($b_{\text{H}_2} = 5$ km s^{-1}), producing an average cross section for Ly α photon absorption $\sigma(\text{H}_2) \sim 10^{-14}$ cm^2 .

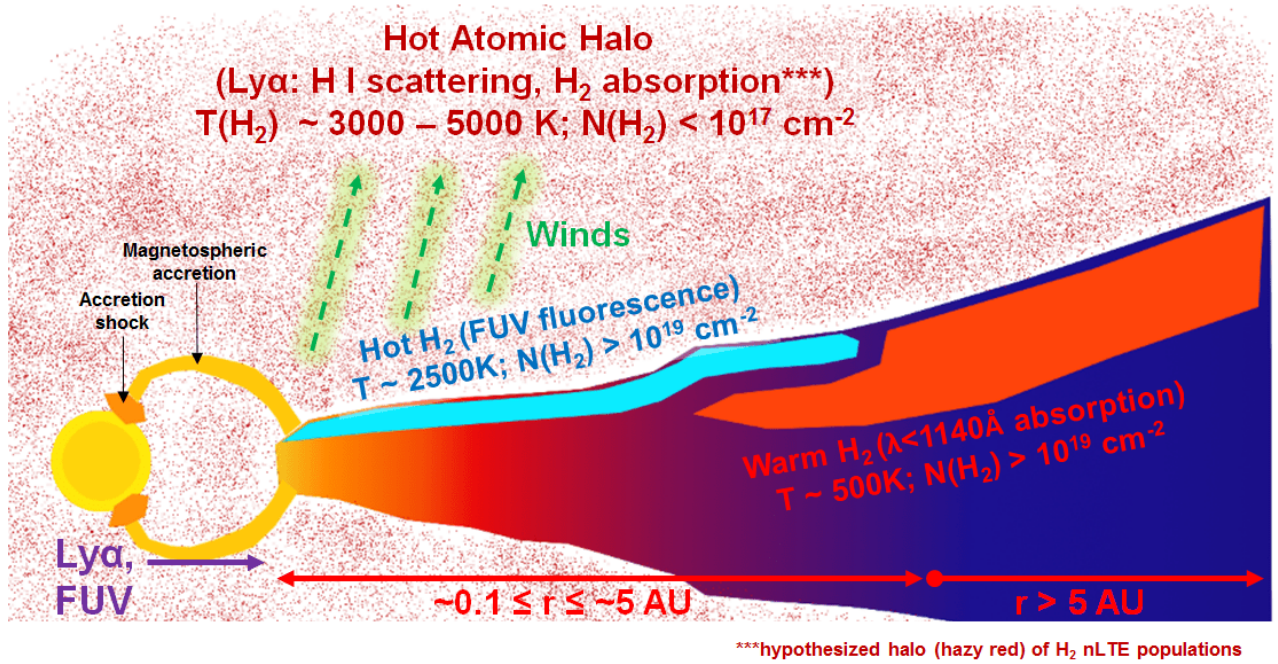


Figure 12. A schematic showing the inner region of the warm PPD and environment. Regions where H_2 is observed as various features are labeled: hot H_2 fluorescence (emission - light blue) appear to come from a layer in the inner disk atmosphere where FUV/X-ray/ $\text{Ly}\alpha$ radiation heat the gas (Ádámkóvics et al. 2016), whereas the H_2 populations observed by France et al. (2014a) in absorption (orange-red) are cooler, indicating a warm layer of molecules probed either further out in the disk than the H_2 fluorescent populations, closer to the disk midplane, or a combination of both. The hot H_2 populations probed against the protostellar $\text{Ly}\alpha$ wings, however, do not appear related to either of the other observed H_2 populations. Instead, we speculate that these hot H_2 populations are probed within a “halo” of hot atomic gas surrounding the protostar+disk (hazy dark red). Since it is difficult to pinpoint a specific region where this gas resides, we include all regions where these H_2 populations may reside, including close to the protostar and/or magnetospheric accretion front from the disk to the star, to regions surrounding the disk, such as hot gas near the disk atmosphere or gas flowing away from PPD as thermal/photoevaporative winds.

We do not include additional losses of $\text{Ly}\alpha$ flux due to absorption from other atomic species, as it is assumed that the dominant constituent of the disk PDR is neutral hydrogen at an average $T_{\text{gas}} \sim 3500 - 5000$ K, which will scatter $\text{Ly}\alpha$ around the region. We can quantify the ratio of the UV photo-excitation rate to the average transition probability for quadrupolar H_2 IR emission lines ($A_{\text{quad}} \sim 10^{-7} \text{ s}^{-1}$; Wolniewicz et al. 1998), $\gamma_{\text{Ly}\alpha} / A_{\text{quad}} \sim 10^4$ photons, meaning that of order 10,000 $\text{Ly}\alpha$ photons are absorbed for every one quadrupolar photon emitted. Therefore, quadrupole emission is not an effective means of cooling the photo-excited H_2 populations in these regions.

Next, we explore what the expected collisional rate between H_2 and other particles in the hot atomic slab must be to balance with the UV photo-excitation rate. First, we set the total collisional rate of all particle interactions with H_2 in this region to match the photo-excitation rate of H_2 in the hot atomic region, such that $\Sigma\alpha_{\text{H}_2,i} = \gamma_{\text{Ly}\alpha} \sim 10^{-3} \text{ collisions s}^{-1}$. Given $\langle N(\text{H}_2) \rangle$ from our empirical models, we estimate the total number density of H_2 in the hot atomic layer to be $n(\text{H}_2) \sim 10^3 \text{ cm}^{-3}$. Finally, we estimate the total collisional rate

with H_2 needed to match the photo-excitation rate of H_2 via $\text{Ly}\alpha$ -pumping, $\Sigma C_{\text{H}_2,i} \sim \Sigma\alpha_{\text{H}_2,i} / n(\text{H}_2) \sim 10^{-6} \text{ cm}^3 \text{ s}^{-1}$.

This result suggests that, at $T_{\text{gas}} \approx 3500 - 5000$ K, interactions between H_2 and dominant particles in the hot atomic environment, like H I, protons (p^+), and electrons (e^-), are expected to occur at a total rate of $\sim 10^{-6} \text{ cm}^3 \text{ s}^{-1}$. Mandy & Martin (1993) and Roberge & Dalgarno (1982) find collisional rates between $\text{H}_2 + \text{H I}$ to be of order $C_{\text{H}_2,\text{HI}} \sim 10^{-10} \text{ cm}^3 \text{ s}^{-1}$ for gas with $T_{\text{gas}} \approx 2000 - 4500$ K (which is similar to interactions between $\text{H}_2 + \text{p}^+$; Black & Dalgarno 1977; Smith et al. 1982). The rate of collisions between $\text{H}_2 + \text{e}^-$, for gas with $T_{\text{gas}} \sim 3500$ K, is found to be $C_{\text{H}_2,\text{e}^-} \sim 10^{-11} \text{ cm}^3 \text{ s}^{-1}$ (Prasad & Huntress 1980). Additionally, interactions between $\text{H}_2 + \text{H}_2$ are expected to occur much less frequently, with $C_{\text{H}_2,\text{H}_2} \sim 10^{-16} \text{ cm}^3 \text{ s}^{-1}$ for $T_{\text{gas}} \sim 3500$ K (Mandy 2016).

We find that the integrated collision rate of H_2 in these environments, derived from literature values, is ~ 4 dex lower than the photo-excitation rate of H_2 by $\text{Ly}\alpha$ radiation alone. When we quantify the ratio of the UV photo-excitation rate to the total collisional rate of par-

ticles with H₂ in this exercise (optimistically assuming $\Sigma C_{H_2,i} \sim 10^{-9} \text{ cm}^3 \text{ s}^{-1}$), $\gamma_{Ly\alpha} / (\Sigma C_{H_2,i} \times n(H_2)) \sim 10^3$ photons, or that $\sim 1,000$ Ly α photons are absorbed for every one de-excitation collision of H₂.

We conclude that it is therefore plausible that "Ly α multiple pumping" may play a key role in re-distributing H₂ rovibrational states in this hot gas region of the circumstellar environment before collisions or rovibrational emission can cool the molecules. Indeed, our simple calculation compliments observed behaviors of H₂ rovibration levels in ISM PDR environments (e.g., [Draine & Bertoldi 1996](#); [Hollenbach & Tielens 1999](#), and references therein). The critical density of most H₂ rovibration levels, or the ratio of the radiative lifetime of a given state (A_{ul} , in s^{-1}) to the collision rate for de-excitation out of the same state ($C_{H_2,i}$, in $\text{cm}^3 \text{ s}^{-1}$), is typically of order 10^4 cm^{-3} for $T_{gas} > 2000 \text{ K}$ ([Mandy & Martin 1993](#)). In our estimation, the density of H₂ is near this critical density, but is still under it, allowing "multiple pumping" to populate H₂ states by UV pumping before collisions de-excite the level populations ([Draine & Bertoldi 1996](#); [Hollenbach & Tielens 1999](#)).

5.2.2. A Simple Model of Ly α -pumped H₂

What, then, is the expected distribution of H₂ rovibration levels if Ly α -pumping plays a significant role in regulating the ground states of the molecules? We create a simple model of H₂ photo-excitation, in the absence of cooling routes (i.e., rovibrational emission and collisional de-excitation), which tracks the column densities of individual H₂ rovibrational levels in the presence of an appreciable Ly α radiation field. This model tracks the fluorescence cascade of H₂ from excited electronic levels, pumped by photo-excitation, back to the ground electronic level until the column densities of rovibration states settles to a preferential distribution, (i.e. the states no longer significantly change due to the photo-excitation process). The framework of the model, which we will refer to as Model 3, is as follows:

1. We start with a thermal distribution of hot H₂, where rovibrational levels are statistically defined by the total column density ($N(H_2)$) and temperature ($T(H_2)$) of the bulk molecular population.
2. A constant, uniform radiation distribution of Ly α photons are generated and exposed to the initially-defined thermal population of H₂.
3. H₂ in the correct $[v,J]$ ground level will have some probability to absorb Ly α photons incident on the H₂ populations. If the H₂ molecules absorb the photons, they are pumped to an excited electronic level, either in the Lyman or Werner bands. From there, they immediately decay back to the ground state in a fluorescent cascade. The probability for a Ly α -pumped H₂ to decay back to a specific ground level is defined by the branching

ratios (transition probabilities) from the excited electronic level $[v',J']$ to the ground electronic level $[v'',J'']$.

4. All rovibration levels of H₂ are followed simultaneously and allowed to redistribute themselves by transition probabilities after initially being photo-pumped out of their original ground electronic level, $[v,J]$. The model runs until the ground rovibration levels settle to a nearly constant distribution of levels in the presence of this unchanging Ly α radiation field.

The Ly α radiation distribution used in Model 3 is assumed to mimic the observed line width and shape on a target-by-target basis. The Ly α line shape is assumed to be Gaussian, with parameters describing the line shape adapted from [McJunkin et al. \(2014\)](#). The flux in the Ly α line, $F_{Ly\alpha}$, is allowed to float in each model run, as are $N(H_2)$ and $T(H_2)$, which set the initial conditions for each model iteration. For the duration of each model, the Ly α line emission is assumed to neither change in shape nor in peak flux, effectively providing the H₂ populations with a constant, uniform distribution of Ly α photons until the H₂ ground states relax to some preferential distribution. The basic mechanics of the model take advantage of ~ 100 H₂ cross sections coincident with the Ly α emission profiles of typical PPD targets (i.e., Classic T Tauri stars; [France et al. 2014b](#)). These cross sections are calculated using intrinsic transition properties of H₂ with Ly α provided by [Abgrall et al. \(1993a\)](#) and [Abgrall et al. \(1993b\)](#). Based on the energy of a given Ly α photon, H₂ in a receptive rovibration level $[v,J]$ will absorb the photon and be pumped to either the Lyman or Werner excited electronic band. The excited H₂ molecules will decay back to one of many potential ground electronic rovibration levels via branching ratio probabilities, again inferred from intrinsic molecular properties provided by [Abgrall et al. \(1993a\)](#) and [Abgrall et al. \(1993b\)](#). This process is repeated until the rovibration levels of H₂ relax to some distribution of states under the constant Ly α flux (i.e., no significant change in the column densities of rovibration levels is detected, to within $\delta \log_{10} N(H_2[v,J]) \lesssim 0.1$ for all rovibration levels). See [Appendix C.1](#) for more details about the models, including the iteration process used for Ly α -pumping, H₂ electronic fluorescence and further details regarding the MCMC and statistics of the process.

We present Model 3 results in [Table 4](#). [Figure 13](#) shows the observed rotation diagram of RW Aur A and the resulting modeled distribution of H₂ rovibration levels produced by Model 3. The Ly α photo-excitation models for all targets are presented in [Appendix 4](#). Green plus symbols represent all H₂ rovibrational states for $v \leq 15$, $J \leq 25$, while cyan "X" symbols represent modeled rovibration levels with the same rovibration level as those empirically measured in the stellar Ly α wings of the target. Model 3 for RW Aur finds a total

Table 4. Ly α -pumped H₂ Column Density & Temperature Results

Target	Model 3			$\Delta N(\text{H}_2)^{a,d}$
	N(H ₂) ^a	T(H ₂) ^b	F _{Lyα} ^c	
AA Tau	16.28 ^{+0.52} _{-0.33}	3214 ⁺⁵⁷⁰ ₋₈₁₀	-10.4 ^{+0.8} _{-0.7}	14.13
AB Aur	15.60 ^{+0.29} _{-0.16}	3437 ⁺⁴¹⁰ ₋₆₉₁	-10.5 ^{+0.5} _{-0.6}	13.44
AK Sco	15.65 ^{+0.50} _{-0.27}	3601 ⁺²⁹⁰ ₋₅₂₂	-10.2 ^{+0.7} _{-0.3}	13.35
BP Tau	17.09 ^{+0.94} _{-0.58}	2557 ⁺¹¹¹³ ₋₁₃₃₉	-6.7 ^{+0.6} _{-0.5}	13.09
CS Cha	18.36 ^{+0.68} _{-1.17}	1596 ⁺¹⁷⁰⁰ ₋₃₄₀	-6.9 ^{+0.3} _{-0.4}	13.61
DE Tau	16.21 ^{+0.45} _{-0.34}	2982 ⁺⁶⁹³ ₋₈₁₂	-9.4 ^{+0.7} _{-0.7}	13.94
DF Tau A	16.48 ^{+1.23} _{-1.38}	2678 ⁺⁹⁴⁰ ₋₁₂₅₈	-6.9 ^{+0.4} _{-4.2}	12.63
DM Tau	16.30 ^{+0.80} _{-0.28}	3670 ⁺²³² ₋₈₈₈	-8.7 ^{+1.0} _{-0.6}	13.90
GM Aur	16.15 ^{+0.32} _{-0.22}	3469 ⁺³⁷⁶ ₋₆₅₀	-7.5 ^{+0.3} _{-0.4}	13.55
HD 104237	17.87 ^{+0.57} _{-0.52}	2200 ⁺¹⁰⁶⁰ ₋₇₆₆	-5.7 ^{+0.2} _{-0.3}	13.25
HD 135344 B	16.78 ^{+0.46} _{-0.31}	3185 ⁺⁵¹⁷ ₋₁₁₂₈	-6.4 ^{+0.3} _{-0.3}	13.26
HN Tau A	16.95 ^{+0.99} _{-0.64}	2140 ⁺¹⁰⁸⁸ ₋₉₉₈	-8.9 ^{+1.5} _{-1.3}	12.24
LkCa15	18.09 ^{+1.00} _{-0.53}	3456 ⁺³⁹⁴ ₋₈₅₈	-8.9 ^{+2.1} _{-1.3}	13.81
RECX 11	16.72 ^{+0.32} _{-0.25}	3087 ⁺⁵⁹³ ₋₄₁₁	-6.7 ^{+0.3} _{-0.7}	13.60
RECX 15	17.13 ^{+0.55} _{-0.53}	2679 ⁺⁹³³ ₋₇₉₈	-5.9 ^{+0.2} _{-0.5}	13.85
RU Lupi	17.26 ^{+0.46} _{-0.47}	2735 ⁺⁶²¹ ₋₉₇₆	-5.7 ^{+0.1} _{-0.4}	13.95
RW Aur A	18.03 ^{+0.68} _{-0.71}	2504 ⁺¹⁴⁸⁹ ₋₆₂₇	-5.6 ^{+0.1} _{-0.2}	14.25
SU Aur	17.59 ^{+1.31} _{-1.20}	2739 ⁺⁸⁵⁷ ₋₁₆₃₁	-6.1 ^{+0.4} _{-4.0}	12.85
SZ 102	16.97 ^{+1.31} _{-0.89}	2662 ⁺⁹⁴⁰ ₋₁₄₃₅	-6.9 ^{+1.0} _{-2.3}	13.16
TW Hya	17.19 ^{+1.22} _{-0.61}	1910 ⁺¹⁵¹⁴ ₋₁₀₂₉	-6.6 ^{+0.6} _{-0.3}	13.03
UX Tau A	17.54 ^{+1.40} _{-0.49}	2734 ⁺⁸⁸⁰ ₋₁₇₈₉	-6.5 ^{+0.8} _{-1.2}	13.75
V4046 Sgr	16.24 ^{+1.05} _{-0.32}	2803 ⁺⁷⁷¹ ₋₁₃₀₉	-6.6 ^{+0.7} _{-1.1}	12.76
Avg. Results	16.93 ^{+1.40} _{-1.33}	2820 ⁺⁸⁵⁰ ₋₁₂₂₄	-7.4 ^{+1.8} _{-3.1}	13.43

^aAll column densities are to the power of 10 ($\log_{10}N(\text{H}_2)$).

^bTemperatures of H₂ (T(H₂)) are in Kelvin.

^cThe integrated Ly α fluxes that pump H₂ populations out of thermal equilibrium are described by the sum of a narrow and broad Gaussian component, with FWHMs of each component adapted from [McJunkin et al. \(2014\)](#). Flux are to the power of 10 ($\log_{10}F(\text{Ly}\alpha)$). F(Ly α) has units of $\text{ergs cm}^{-2} \text{s}^{-1}$.

^dThe integrated residual between the observed column densities of H₂ in states $[v, J]$ to the model prediction of column density in the same rovibrational levels, $\Sigma|N(\text{H}_2[v, J])_{data} - N(\text{H}_2[v, J])_{model}|$.

column density of H₂, $\log_{10}(N(\text{H}_2)) \approx 18.0$, which is ~ 2 dex lower than results from [France et al. \(2014b\)](#), at a temperature $T(\text{H}_2) \approx 2500$ K (in [France et al. \(2014b\)](#), $T(\text{H}_2)_{warm} = 440$ K).

The total column density of thermal H₂ for RW Aur is slightly larger than the average best-fit $N(\text{H}_2)$ for all targets ($\langle \log_{10}N(\text{H}_2) \rangle \sim 17.0$), with the smallest total column density $\log_{10}N(\text{H}_2) \approx 15.5$. Interestingly, for almost all samples in our survey, the derived total column density of thermal H₂ distributions is larger than those estimated by our thermal models (i.e., Models 1 and 2). For all targets, the derived thermal temperatures of H₂ from the Ly α -pumping model range from 1500 - 4000 K ($\langle T(\text{H}_2) \rangle \sim 2800$ K). Overall, the final results from the Ly α -pumping models overestimate the total column density of H₂ for a hot atomic layer origin by ~ 1 -2 dex and underestimate the total column density of H₂ for a warm molecular layer origin by the same amount ([Ádámkóvics et al. 2016](#)). Additionally, the temperature of thermal H₂ is found somewhere between the two layers.

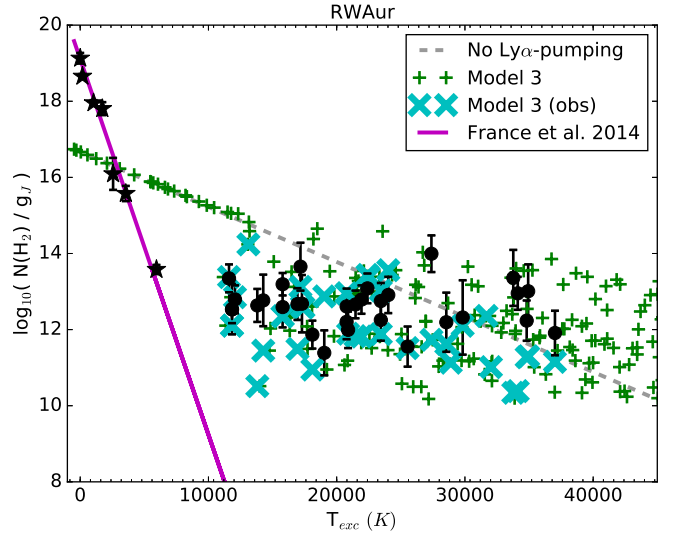


Figure 13. The rotation diagram for RW Aur, with rovibrational column densities derived in this study (black circles) and lower energy states calculated by [France et al. \(2014a\)](#) (black stars; $\lambda\lambda$ 1092.5 – 1117 Å). The magenta solid line shows the thermal distribution H₂ levels examined by [France et al. \(2014a\)](#), with $\log_{10}(N(\text{H}_2)) = 19.90 \text{ cm}^{-2}$ and $T(\text{H}_2) = 440$ K. The green plus symbols represent the H₂ rovibrational levels output by the Ly α -pumping models (Model 3). The cyan “X”s mark rovibrational levels from Model 3 which match the observed H₂ levels, so the reader can directly compare the the data with the modeled states. The gray dashed line presents the initial thermal distribution of H₂ in the models (i.e., without Ly α pumping), which is described by $\log_{10}(N(\text{H}_2)) = 18.03$ and $T(\text{H}_2) = 2504$ K.

One of the first things we notice about the Model 3 results is that the H₂ rovibrational levels are redistributed in such a way that more highly excited H₂ levels ($T_{exc} \gtrsim 30,000$ K) can be pumped to higher column densities than they are expected to be in thermal distributions. Rovibrational levels of H₂ most affected by the flux of Ly α (i.e., $v \geq 2$; $T_{exc} \sim 10,000$ K) first appear diminished in column density, relative to the native thermal distributions, but for rovibrational levels with $T_{exc} \gtrsim 30,000$ K, the relative column densities of highly energetic states appears to return back towards the level of the thermal distribution, with many states being pumped by $\gtrsim 1$ dex more than they would otherwise be in thermally-distributed states.

Additionally, the re-distributed H₂ rovibrational levels appear scattered, with the behavior of the scattered distributions appearing roughly consistent for rovibrational levels with $T_{exc} \gtrsim 10,000$ K and with a spread of ~ 1 dex. We note that this behavior matches the characteristic distributions of empirically-derived H₂ rovibration levels measured against Ly α for most, if not all, of our PPD sightlines. The Ly α redistribution appears to scatter most H₂ states out of thermal equilibrium at $T_{exc} \gtrsim 10,000$ K, suggesting that the H₂ absorption coincident on the Ly α wings do not probe thermal populations of H₂ in these sightlines. The fact that we see this same peculiar H₂ population behavior for all disks in our survey, regardless of orientation of the disk in the line of sight (i.e., i_{disk}), suggests that the sampling of H₂ may not be co-spatial with the same H₂ populations observed in fluorescence from each disk. The models also suggest that, for rovibrational levels insensitive to Ly α radiation (i.e., $v < 2$), H₂ may still be thermally populated. Theoretically, if we could observe rovibrational levels of H₂ not pumped by Ly α radiation, we could test this hypothesis.

We do have one case study - RW Aur - where this test is currently possible. The sightline to RW Aur probes both hot H₂ embedded in the Ly α profile of the protostar and warm H₂ in the FUV continuum ($\lambda\lambda$ 1090 - 1120 Å; France et al. 2014b). If the warm disk H₂ populations and the hot Ly α H₂ populations were co-spatial with one another, we would expect to find signatures in the FUV-continuum probing the same hot H₂ population (specifically for $v = 0$, $J = 4, 5, 6$; $\lambda = 1100.2, 1104.1, 1104.5, 1109.3, 1109.9, 1115.5, 1116.0$ Å, where the distributions of warm and hot H₂ populations overlap). From the Ly α -pumping model results for RW Aur, we expect to find appreciable thermal columns of hot H₂ in the sightline, which is several dex denser than the warm H₂ probed by the FUV continuum. The FUV continuum is much less likely to scatter through the gas disk than Ly α , and therefore is expected to provide a better probe of the geometry through the disk material. The fact that the France et al. (2014b) study does not see clear deviations to the larger column density found by Model 3 for hot H₂[$v = 0$, $J = 4, 5, 6$] in the FUV con-

tinuum is further evidence supporting our original hypothesis - that the resonance nature of Ly α allows the radiation to scatter through a hot atomic halo above the PPD, and the observed H₂ signatures observed in the protostellar Ly α wings probe residual H₂ in these environments, rather than in the disk.

6. CONCLUSIONS

We perform the first empirical survey of H₂ absorption observed against the stellar Ly α emission profiles of 22 PPD hosts. The aim of this study was to identify thermal and non-thermal H₂ species in each sightline and investigate excitation mechanisms responsible for the distributions of non-thermal H₂ populations. We normalize each Ly α profile and create optical depth models to synthesize H₂ absorption features observed across the normalized Ly α spectra. Each optical depth model estimates the column density of H₂ in ground states [v, J] from the absorption depth in the Ly α wings, and we present the H₂ rotation diagrams of all samples in our survey to examine the behavior of the H₂ rovibrational populations in all sightlines. Below, we highlight our findings and conclusions:

- Thermally-distributed H₂ models alone cannot reproduce observed rovibration levels. Highly-energetic states are “pumped” when compared with lower energy rovibrational states. This appears to happen at “knee” junctures, which are consistently found at $T_{exc} = 20,000$ K, 25,000-26,000 K, and 31,000-32,000 K.
- We find roughly-equivalent total column densities of thermal and non-thermal H₂ populations in transitional disk samples and samples with detectable C IV-pumped H₂ fluorescence. Primordial disk targets have more spread in this relation, and show more samples with larger total column densities of thermal H₂ than non-thermal H₂ populations.
- High energy continuum radiation, produced primarily by accretion processes onto the host protostar, appears to play an important role in regulating the total density of non-thermal H₂ in the circumstellar environment. We find correlations between the X-ray and FUV luminosities and $N(\text{H}_2)_{\text{nLTE}}$ and little evidence that line emission from protostellar accretion processes plays a significant role in regulating the total column densities of thermal and non-thermal H₂ states, except C IV, which appears to be anti-correlated with the total thermal column densities of H₂.
- There is a clear anti-correlation between $N(\text{H}_2)_{\text{nLTE}}$ and H₂ dissociation continuum, suggesting that photo-excitation may be more effective at unbinding H₂ already in highly energized levels than lower energy thermal states.

- From one target that has access to cooler H₂ populations observed against the FUV continuum (RW Aur A; France et al. 2014b), we see two populations of H₂: warm H₂ probing higher density material in the protoplanetary disk, and hot H₂ in an atomic halo surrounding the protostar and disk. The total column of warm H₂ is several dex higher than the total column of hot H₂ in the Ly α wings. We see a crossing point, where we should begin to see warmer columns of H₂ in the FUV continuum ($T_{exc} \approx 3,000$ K), but, observationally, this does not appear to be the case. H I-Ly α is a strong resonance transition, and a small amount of residual H I in the protostellar environment will scatter Ly α before it escapes. We suspect that the H₂ populations probed in the protostellar Ly α wings are not associated with the disk, but rather found in a tenuous halo of hot, mostly atomic gas around the disk. The hot H₂ also probes much lower column densities ($\langle N(\text{H}_2) \rangle \sim 10^{16} \text{ cm}^{-2}$) of H₂ than is required to produce the observed fluorescence in these same PPD samples, strongly suggesting that absorption and fluorescence H₂ populations are not co-spatial.

While this study examined the behavior of hot H₂ in protoplanetary disk environments, further investigation and proper implementation of non-LTE models is necessary to pinpoint the physics driving H₂ to higher $[v, J]$ states. Studies have been performed that point to several mechanisms driving H₂ populations, including collisions with other particles and higher energy photons (FUV/EUV/X-ray; Nomura et al. (2005); Nomura & Millar (2005); Ádámkóvics et al. (2016)) and reformation/destruction of H₂ by chemical evolution, especially H₂O dissociation in the warm disk atmosphere (Du & Bergin 2014; Glassgold & Najita 2015). The next step forward would be to implement radiative, collisional, and chemical processes simultaneously to simulate the PPD environmental behavior. Paper II will address the spatial origins of this H₂ absorption, based on results from this study and empirical evidence from the absorption features themselves.

This research was funded by the NASA Astrophysics Research and Analysis (APRA) grant NNX13AF55G, *HST* GO program 12876, *HST* GO program 13372, and *HST* AR program 13267, and uses archival NASA/ESA *Hubble Space Telescope* observations, obtained through the Barbara A. Mikulski Archive for Space Telescopes at the Space Telescope Science Institute. The authors thank the anonymous referee for their helpful feedback, which ultimately improved the quality of this paper. KH would like to thank Allison Youngblood, Ilaria Pascucci, Andrea Banzatti, and Klaus Pontoppidan for enjoyable discussion and constructive suggestions.

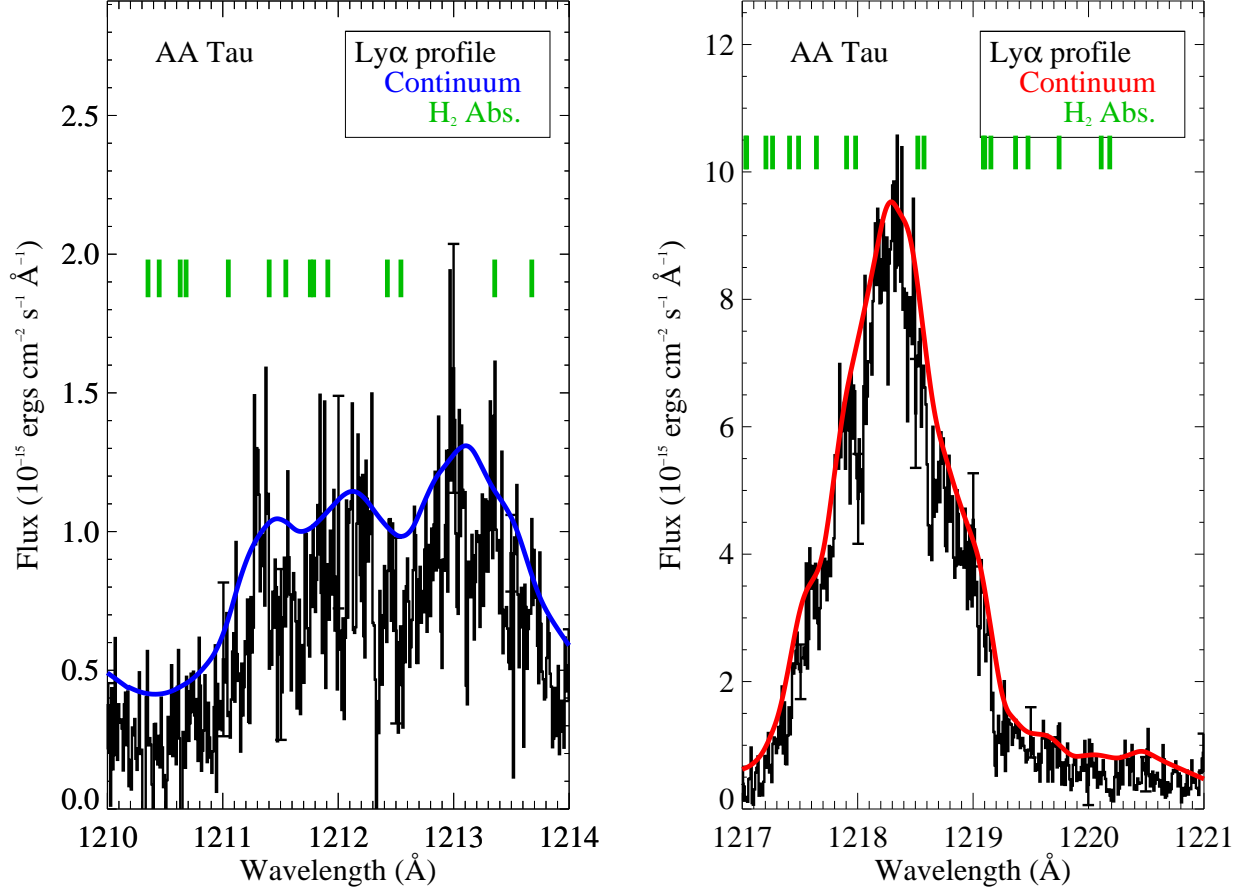


Figure 1. The Ly α profiles of each target, overlaid with the Ly α “continuum” fit determined from our functional processes (Section 3). Two targets are shown per row, where the blue and red Ly α profiles are presented. The Ly α mean flux arrays are over-plotted in blue (over the blue-wing Ly α component) and red (over the red-wing Ly α component). We mark the location of H₂ absorption transitions in the Ly α profiles with green hashes. The continuum fit is determined to normalize the Ly α emission profile, which is achieved by dividing the mean flux continuum through the emission line, creating a normalized spectral region across the Ly α wing.

APPENDIX

A. ADDITIONAL DETAILS ON H₂ ABSORPTION LINE ANALYSIS

Fig. Set 1. The Ly α profiles of each PPD host

Information about each H₂ absorption transition was found either in [Abgrall et al. \(1993a\)](#) or [Abgrall et al. \(1993b\)](#), specifically the Einstein A-coefficient, describing the rate of spontaneous decay from state $u \rightarrow l$ (A_{ul}), and the wavenumber. All H₂ transitions were selected from [Roncin & Launay \(1995\)](#) between 1210 - 1221 Å, with transitions preferentially considered from those previously called out by [Herczeg et al. \(2002\)](#) and [France et al. \(2012a\)](#). Other H₂ transitions included in the line-fitting analysis met a minimum (A_{ul}) $\geq 3.0 \times 10^7 \text{ s}^{-1}$, to ensure that the absorption transition probabilities were large enough for detection, assuming a warm thermal population of H₂. The energy levels of ground state H₂ in vibration and rotation levels [v, J] (E_{gr}) were derived from equations outlined in [H₂ools \(McCandliss 2003\)](#), with physical constants taken from [Herzberg \(1950\)](#), [Jennings et al. \(1984\)](#), and [Draine \(2011\)](#). The physical properties of the H₂ transition were derived from intrinsic properties of the molecule:

$$\sigma(\lambda) = \left(\frac{\lambda_\lambda^3}{8\pi c} \right) \left(\frac{g_u}{g_l} \right) A_{ul} \quad (\text{A1})$$

$$f_{lu} = \left(\frac{m_e c}{8\pi^2 e^2} \right) \left(\frac{g_u}{g_l} \right) \lambda_{lu}^2 A_{ul} \quad (\text{A2})$$

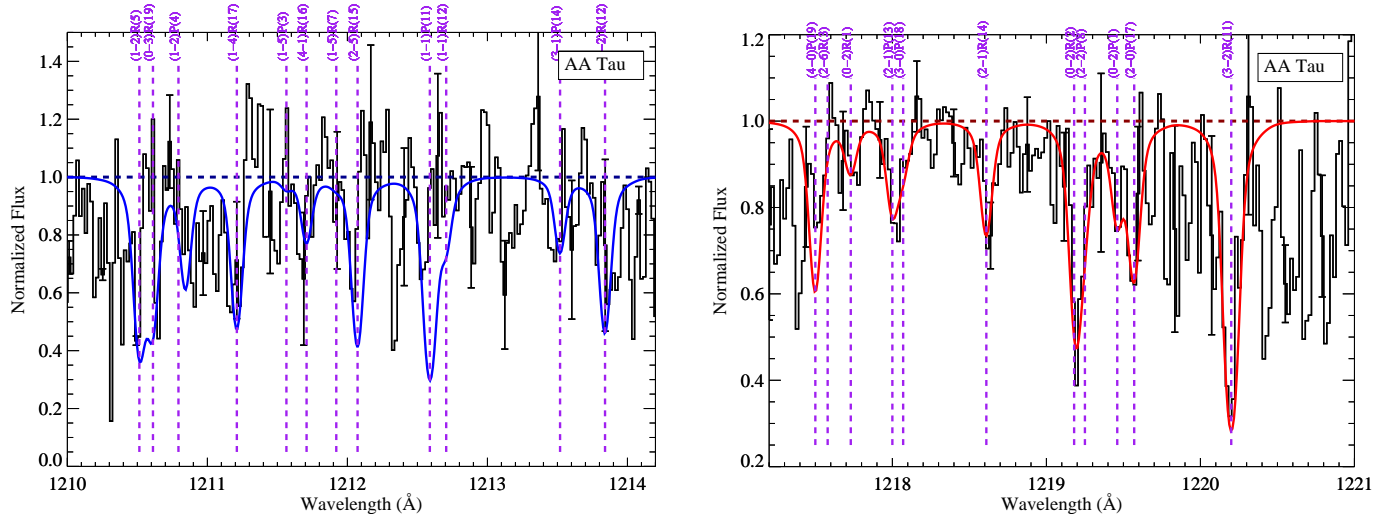


Figure 2. The final, synthesized absorption spectra of warm H_2 against the $Ly\alpha$ transmission spectra. For targets that have transmission spectra for both blue and red $Ly\alpha$ wings, blue wing spectra are shown on the *left* (blue H_2 absorption fit) and red wing spectra are on the *right* (red H_2 absorption fit). For targets with only a red-wing transmission spectrum, red-wing fits are shown on the *left* (red H_2 absorption fit).

where λ_λ is the photo-excitation wavelength, $Ly\alpha$, of H_2 in ground state $[v, J]$; g_u and g_l are the statistical weights of the electronically-excited $[v', J']$ and ground $[v, J]$ states, respectively; and $(\pi e^2/m_e c)$ is the definition of the classical cross section, expressed as $0.6670 \text{ cm}^2 \text{ s}^{-1}$ in cgs units. Table 2 shows all transitions used in our H_2 synthetic absorption model, including physical properties (E_{gr} , f_{lu} , A_{ul}) and level transition information. Not all transitions were implemented for every target. Depending on the effective range of the stellar $Ly\alpha$ wing in wavelength space, many of the transitions found on the edges of the wings (1210 – 1212: 1213.5 – 1215.2 Å for the blue wing; 1216 – 1218: 1219.5 – 1221 Å for the red wing) were omitted.

The modeled b-value is fixed in all synthetic absorption spectra to replicate the thermal width of a warm bulk population of H_2 ($T(H_2) \geq 2500 \text{ K}$) in the absence of turbulent velocity broadening. If the b-value were larger, the broadening acts to widen the absorption feature and diminish the depth of the line center, which causes degeneracy between the estimated rovibrational $[v, J]$ level column densities and the thermal/turbulent parameters of the models. When we increased $b_{H_2} = 10 \text{ km s}^{-1}$, the column densities of the rovibrational $[v, J]$ levels were systematically reduced by 0.1-0.7 dex for all survey samples.

The multi-component fit of H_2 absorption was mostly insensitive to initial conditions. Initially, we set the same initial conditions for the start of the run ($v_r = 0 \text{ km s}^{-1}$; $T(H_2) = 2500 \text{ K}$; $\log_{10} N(H_2; v, J)$ varied by transition properties) and allowed the parameters float. Once an effective range of values was determined for all targets, $T(H_2)$ and b_{H_2} were fixed, and only v_r was allowed to float. This produces column density estimates that are relatively comparable for all targets in our survey.

As discussed in France et al. (2012a), only the (0-2)R(2) and (2-2)P(9) levels, whose wavelengths differed by $\Delta\lambda = 0.01 \text{ \AA}$ (at 1219.09 and 1219.10 Å, respectively), were sensitive to the initial conditions. The total column density at this wavelength range is robust, while the relative columns shared between the two transitions was not. To mitigate this, we weighed the individual columns by the product of their oscillator strengths and relative populations of the two levels at $T(H_2) = 2500 \text{ K}$. Using the methodology laid out in H_2 001s and Equation A2, we calculate the oscillator strengths and relative populations of the two lines to be $[f_{R(2)} = 25.5 \times 10^{-3}$; $P_{R(2)} = 5.76 \times 10^{-4}]$ and $[f_{R(9)} = 31.8 \times 10^{-3}$; $P_{R(9)} = 6.24 \times 10^{-4}]$, respectively. Therefore, $N(2,2)$ contributes 0.425 of the total column density determined at 1219.10 Å, while $N(2,9)$ contributes 0.575 of the total column. Column 2 of Figure 2 show the minimized multi-component synthetic spectra plotted over the normalized $Ly\alpha$ wings for the red-ward and blue-ward profile components, respectively.

Fig. Set 2. The Relative Absorption Spectra and H_2 Optical Depth Models of each PPD host $Ly\alpha$ emission wing.

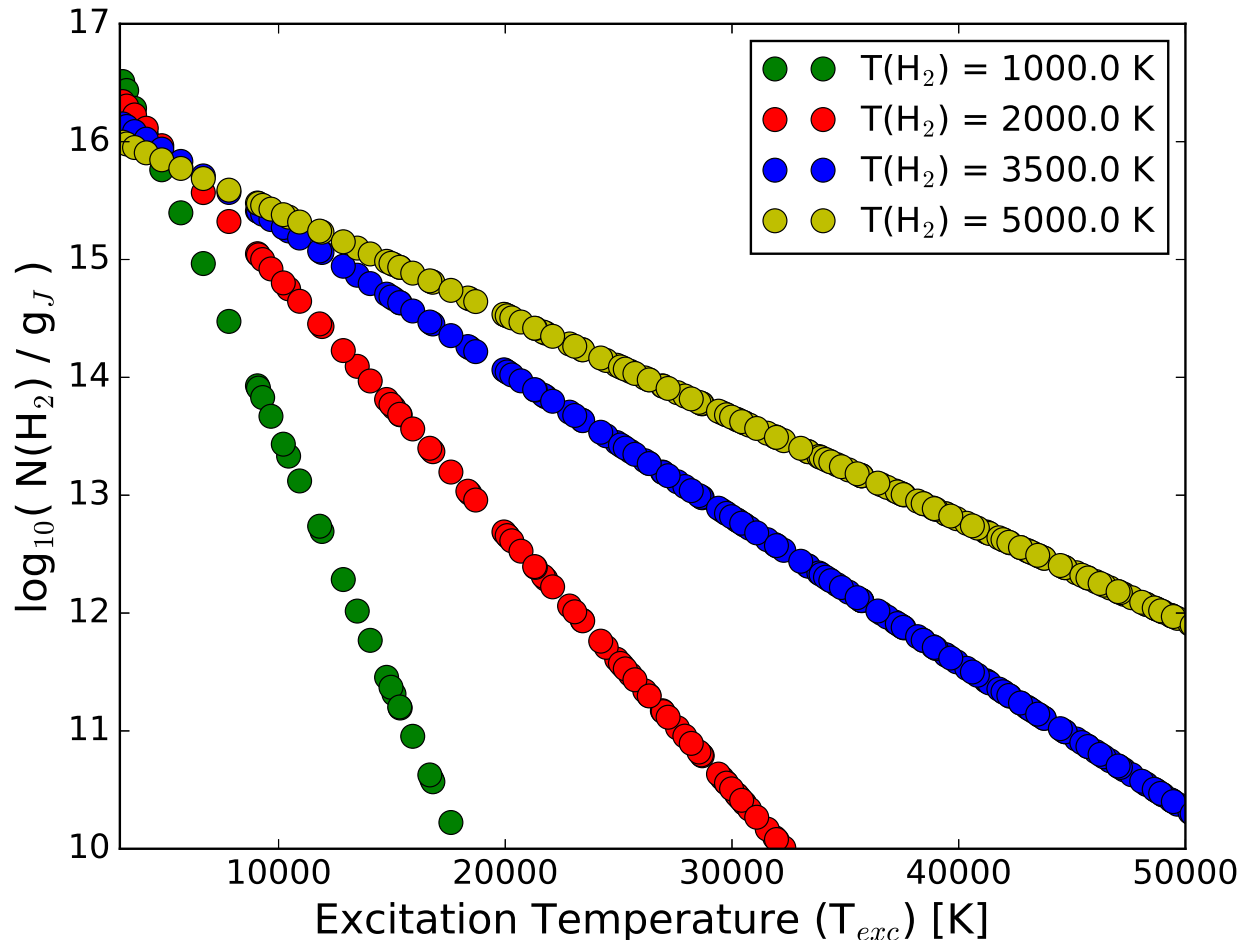


Figure 14. Modeled rotation diagram of H₂ populations found in thermal equilibrium with a set $N(\text{H}_2) = 10^{17} \text{ cm}^{-2}$ and varying thermal descriptions $T(\text{H}_2)$. As $T(\text{H}_2)$ increases, more H₂ populations with higher excitation temperatures, T_{exc} , become populated, increasing the relative ratio of higher T_{exc} state to lower T_{exc} states, which decreases the slope of the distribution towards zero. This model is used to compare the observed rotation profiles of H₂ to thermally-populated states of H₂ for Models 1 and 2.

B. H₂ MODEL DETAILS AND MONTE CARLO SIMULATIONS

B.1. Models 1 & 2: Thermal H₂ Populations only

Models 1 and 2 are simple models that follow the H₂ool1s layout: Given the derived column densities for observed H₂ ground states against the stellar Ly α wing $N(\text{H}_2;v,J)$, we use first principles molecular physics to determine the theoretical population column densities of a bulk H₂ population $N(\text{H}_2)$ described by a shared thermal profile $T(\text{H}_2)$. The level column densities are calculated using Boltzmann populations, assuming LTE conditions, and each ground state energy level is determined by calculating the electronic, vibrational, and rotational energy levels for a ground state $[v,J]$, as described in McCandliss (2003).

Model 1 assumes that all data points extracted from the absorption features of each target are thermally-populated. Model 2 assumes only H₂ populations with ground state energies $E_{gr} < 1.5 \text{ eV}$ ($T_{exc} \lesssim 17500 \text{ K}$) are thermally-populated, with the possibility that H₂ in ground states with $E_{gr} > 1.5 \text{ eV}$ are pumped additionally by some unknown non-thermal process(es), and so are not considered in the model-data comparison. We use Model 2 as a baseline of the minimum $N(\text{H}_2)$ and $T(\text{H}_2)$ of thermal H₂ in the disk atmosphere for each target, assuming any of the observed, absorbing H₂ against the Ly α wing is purely thermally excited.

Figure 14 shows an example of how the relative $[v,J]$ states are populated by the thermal distribution of H₂. While the total column density of H₂ regulates the column densities of H₂ found in ground state $[v,J]$, $T(\text{H}_2)$ determines the relative abundances of each $[v,J]$ to others in the ground state. For example, a lower $T(\text{H}_2)$ means that, statistically, more H₂ is found in ground states with low $[v,J]$ because the overall excess energy in the H₂ populations is low.

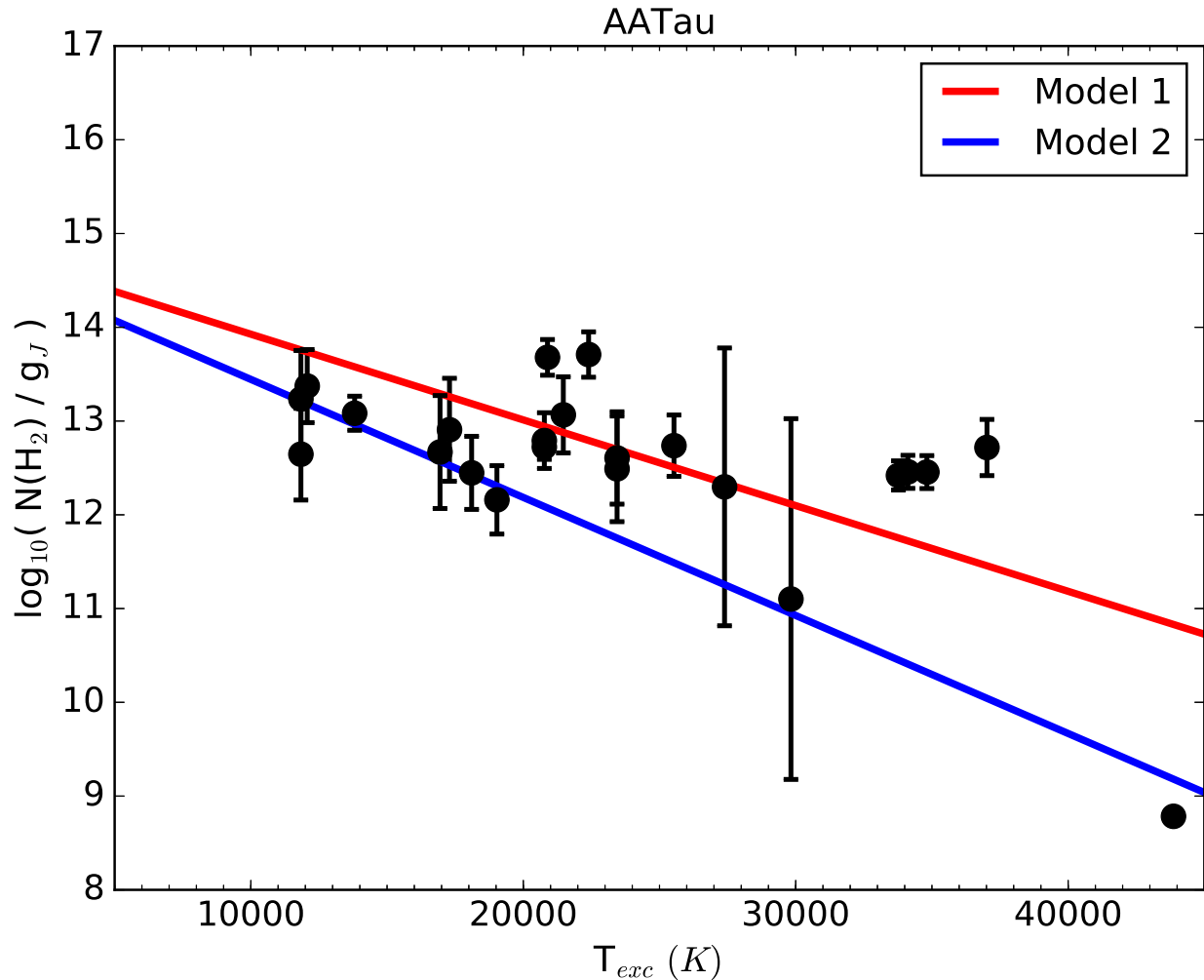


Figure 3. All rotation diagrams are presented here. Each H_2 ground state column density is weighed by its statistical weight, g_J . Model 1 attempts to fit one thermally-populated bulk H_2 population through all data points extracted from the *HST* data sets. Model 2 does the same as Model 1, but only for H_2 states with lower energy ground states ($E_{gr} \leq 1.5$ eV; $T_{exc} \leq 17,500$ K).

However, as $T(\text{H}_2)$ increases, the ratio of the abundances of H_2 found in higher $[v, J]$ states to those in low $[v, J]$ states increases. This appears as a “flattening” of the slope of H_2 populations in Figure 14.

Fig. Set 3. Fitting Thermal Models to Each H_2 Rotation Diagram

C. MCMC SIMULATIONS

Each model is compared to the resulting rotation diagrams derived from the relative H_2 absorption column densities derived as explained in Section 3. This is done using a MCMC routine, which randomly-generates initial parameter conditions and minimizes the likelihood function ($\ln \mathcal{L}(x, \theta)$) between the H_2 rovibration column densities and model parameters. We define $\ln \mathcal{L}(x, \theta)$ as a χ^2 statistic, with an additional term to explore the weight of standard deviations on each rovibrational column density:

$$\ln \mathcal{L}(x, \theta, f) = \frac{(y(x) - y(x, \theta))^2}{\sigma^2} - \ln((\sigma^2 + y(x, \theta)^2 \exp(2f))^{-1}) \quad (\text{C3})$$

In Equation C3, x represents the ground state energy of H_2 in rovibration level $[v, J]$, $y(x)$ is the observed column density of H_2 , $y(x, \theta)$ is the modeled column density of H_2 derived from the thermal model, σ^2 is the variance in the column densities, and f is an estimation on the accuracy of the column density standard deviations. For parameters shared between all thermal model runs ($N(\text{H}_2)$, $T(\text{H}_2)$, $\ln f$), we set prior information about each to keep the model outputs physically viable. We let the total thermal H_2 column density range from $N(\text{H}_2) = 12.0 - 25.0 \text{ cm}^{-2}$. Below

$N(\text{H}_2) = 12.0 \text{ cm}^{-2}$, there is not enough column in individual rovibrational levels to produce measurable absorption features in the data. Additionally, $N(\text{H}_2) \geq 25.0 \text{ cm}^{-2}$ will significantly saturate the features in the absorption spectra, which we do not see for any target in our survey. The thermal populations of H₂ are allowed to range from $T(\text{H}_2) = 100 - 5000 \text{ K}$. The H₂ populations must be warm enough to populate the correct rovibrational levels that absorb Ly α photons, while simultaneously cooler than the dissociation temperature of H₂ ($T(\text{H}_2)_{diss} \approx 5000 \text{ K}$).

For Models 1 and 2, MCMC simulations were run with 300 independent initial randomly-generated parameter realizations (walkers) and allowed to vary over 1000 steps to converge on the best representation of the observations.

C.1. Model 3: Thermal H₂ Populations Photo-excited by HI-Ly α

Model 3 uses the same thermal populations of Models 1 and 2 and adds an additional photo-pumping mechanism to show how thermal populations reach an equilibrium state in the presence of an external radiation field. First, because we observe H₂ absorption against the Ly α wings of these targets and Ly α radiation makes up the vast majority of the FUV radiation that photo-excited H₂ to fluorescence, we assume the radiation pumping the thermal states to new equilibrium populations is dominated by Ly α . To describe the amount of radiation being absorbed by H₂, we add two additional parameters that describe the flux input to the system, $F_n(\lambda)$ and $F_b(\lambda)$, which represent a narrow and broad flux component from the stellar Ly α radiation incident on the H₂ populations. Following the results and analysis from [McJunkin et al. \(2014\)](#), we assume the Ly α radiation profile incident with the H₂ on the disk surface is described by two Gaussian components - a narrow component, where the bulk of the flux is located, and a broad component, which describes the shape of the observed outer wings. [McJunkin et al. \(2014\)](#) find full width at half maximum (FWHM) fits for both the narrow and broad Gaussian components of the radiation distribution, and we use those results to describe the width of our input flux. We allow the peak fluxes of both the narrow and broad flux distributions to vary and have final input Ly α flux distributions described by:

$$\begin{aligned} F_{\text{Ly}\alpha}(\lambda) &= F_n(\lambda) + F_b(\lambda) \\ &= F_n \exp\left(\frac{-\Delta\lambda^2}{2\sigma_n^2}\right) + F_b \exp\left(\frac{-\Delta\lambda^2}{2\sigma_b^2}\right), \end{aligned} \quad (\text{C4})$$

where F_n and F_b are free parameters in the models, and σ_n and σ_b are derived from the FWHM found in [McJunkin et al. \(2014\)](#), and $\Delta\lambda = \lambda - \lambda_{lab}$, where λ_{lab} is the rest wavelength of HI-Ly α (1215.67 Å). Each flux distribution is kept constant throughout the model run, assuming the output radiation from the star over the time it takes to equalize the photo-pumped populations of H₂ is isotropic. We assume $F_n(\lambda)$ and $F_b(\lambda)$ are observed flux rates, and we therefore infer the flux back to the star by reddening the flux with ISM extinction values determined by [McJunkin et al. \(2014\)](#). The allowed ranges of observed total Ly α flux are outlined in [Schindhelm et al. \(2012\)](#) for reconstructed Ly α profiles seen in at the PPDs. We constrain the Ly α flux to $\log_{10}(F_n(\lambda)) = -13$ to $-5 \text{ ergs cm}^{-2} \text{ s}^{-1}$ and $\log_{10}(F_b(\lambda)) = -16$ to $-5 \text{ ergs cm}^{-2} \text{ s}^{-1}$, which are integrated over each Gaussian function in Equation C4.

Once flux and thermal H₂ population parameters are chosen, we follow the change in thermal populations in states $[v, J]$ of H₂ being exposed to the pumping radiation in time iterations of the pumping process, t_{step} , where each t_{step} is considered over some arbitrary Δt . First, we find how much H₂ in state $[v, J]$ is lost to be pumped to some electronic excited state $[v', J']$ because of the interaction with a discrete Ly α photon with wavelength λ . We determine how much H₂ is photo-excited by λ by calculating the cross section for absorption of photon λ , given the transition probabilities of the H₂ rovibration levels. Once all $[v, J]$ state losses via λ absorption have been determined, we allow the excited state H₂ to fluoresce back to the ground state via the branching ratios, or transition probabilities, to some final ground state $[v'', J'']$.

For this simple model, we assume that dissociation of H₂ molecules by Ly α -pumping is negligible. As [Dalgarno & Stephens \(1970\)](#) describe, nearly all Ly α -pumped excited states have bound de-excitation levels, such that transitions from the Lyman band are expected to have very low probabilities of dissociation. While there exist a handful of Werner-band transitions, which likely pose the greatest probability for molecular dissociation upon decay, this simple model does not contain a source term of H₂, such that we cannot control the formation of H₂ at any point in the model. To keep the modeled distributions of H₂ constant throughout the simulated experiment, therefore, we assume that all H₂ transitions result only in the decay of H₂ to arbitrary ground states, with no probability that H₂ dissociates via these fluorescence routes.

This process is repeated until the H₂ populations reach a steady-state equilibrium, such that the absorption out of state $[v, J]$ equalizes with the cascade back to $[v'', J'']$. For $T(\text{H}_2) \leq 5000 \text{ K}$, this equilibrium is reached by $t_{step} = 1000$. With higher $N(\text{H}_2)$, we find that it takes more t_{step} to reach equilibrium, but for $N(\text{H}_2) < 10^{20} \text{ cm}^{-2}$ and high $T(\text{H}_2)$, an equilibrium state is reached after $t_{step} \approx 3000$ steps. Figure 15 shows how the distributions of thermal H₂ populations change when exposed to a constant Ly α flux from the host star, as a function of time steps from first exposure. If we assume the distributions of H₂ ground states are primarily affected by photo-pumping via Ly α photons

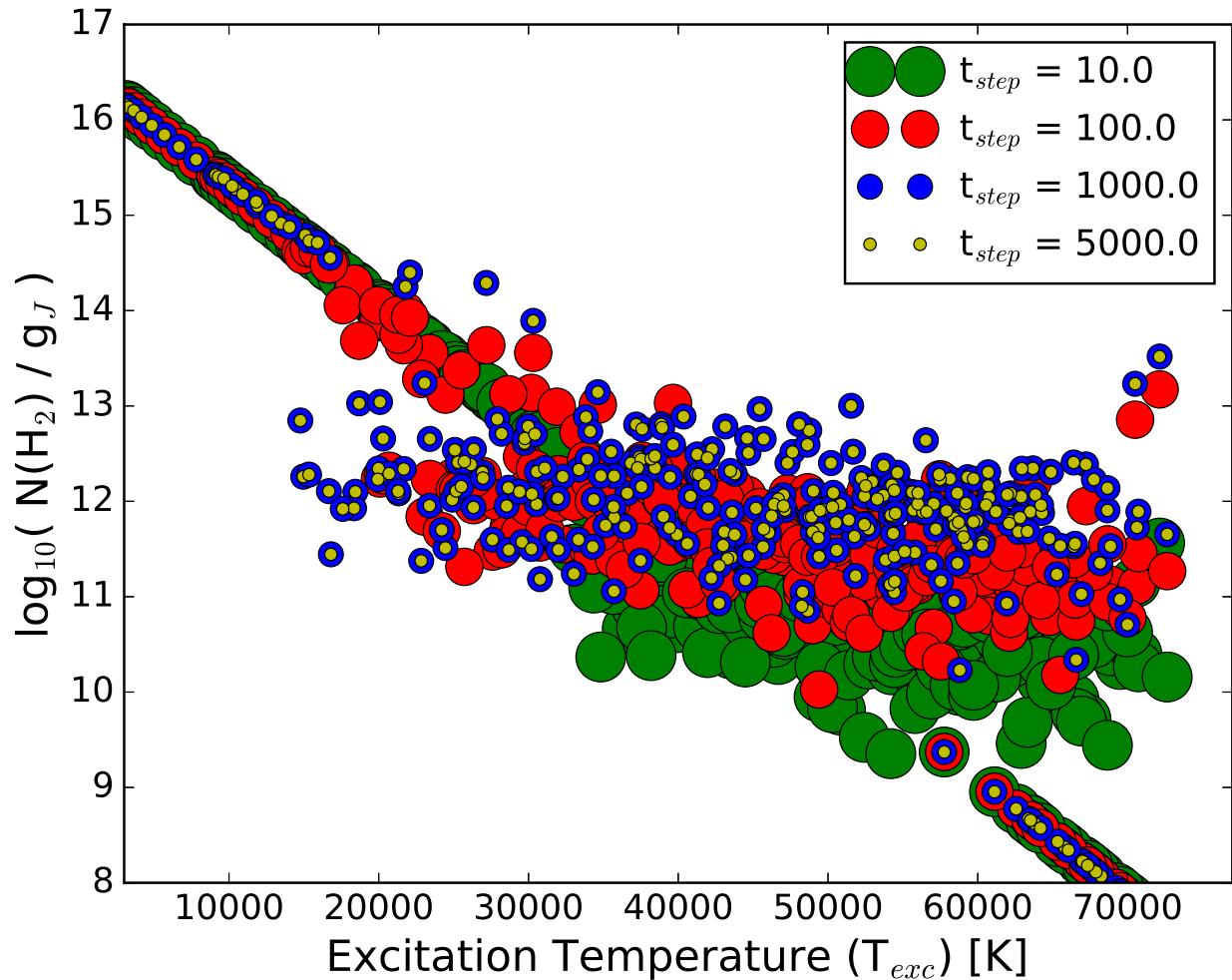


Figure 15. Modeled thermal distributions of H_2 with $N(\text{H}_2) = 10^{17} \text{ cm}^{-2}$ and $T(\text{H}_2) = 3500 \text{ K}$, assuming thermal populations of H_2 are constantly photo-excited by an external $\text{HI-Ly}\alpha$ radiation field to an equilibrium state. The $\text{Ly}\alpha$ radiation field is assumed to be Gaussian in shape when interacting with H_2 molecules, with a peak flux of $10^{-9} \text{ ergs cm}^{-2} \text{ s}^{-1}$ at 1215.67 \AA . We show how the number of iterations of time the H_2 is exposed to the $\text{Ly}\alpha$ flux affects the distribution of H_2 ground states. We find that iterations $t_{step} = 1000$ reaches a final equilibrium state. The thermal distribution + $\text{Ly}\alpha$ pumping mechanics are used to calculate theoretical H_2 populations in Model 3.

and no other physical mechanisms to drive the populations to non-LTE states (collisions with other species, chemical evolution, etc), then equilibrium of H_2 states is reached fairly quickly and does not change from the final equilibrium state of populations.

We perform the same MCMC data-model reduction for Model 3 and the observed rotation diagrams. Model 3 required time iterations and, therefore, took longer to run. We ran two separate iteration of Model 3, the first MCMC simulation having 100 independent walkers varying over the parameter space iterating over 2000 steps with 1000 time iterations of the $\text{Ly}\alpha$ -pumping. We determined that, after about 100 converging steps for each walker, we were able to settle into the best realization of the data. We also determined that longer time iterations were necessary to settle the $\text{Ly}\alpha$ -pumping mechanism into equilibrium for larger column densities ($N(\text{H}_2) > 10^{20} \text{ cm}^{-2}$) and temperatures ($T(\text{H}_2) > 4500 \text{ K}$). We ran a second iteration of MCMC simulations for Model 3 using $t_{step} = 5000$ per model realization, with 100 independent MCMC walkers iterating over 500 steps to convergence. Because of the extensive computation time of Model 3 with 5000 time steps per model realization, we chose to cut the total number of convergence steps to keep the same number of walker realizations in the MCMC.

Table 4 presents parameter results for all modeled H_2 thermal distributions. For all Model 3 realizations, $F_b(\lambda)$ has been excluded, since the majority of the integrated flux of $\text{Ly}\alpha$ is dominated by $F_n(\lambda)$ ($F_n(\lambda) \gg F_b(\lambda)$). Figure ?? shows the best-fit, median model parameters for Model 3 with observed rovibration H_2 levels overplotted. We mark

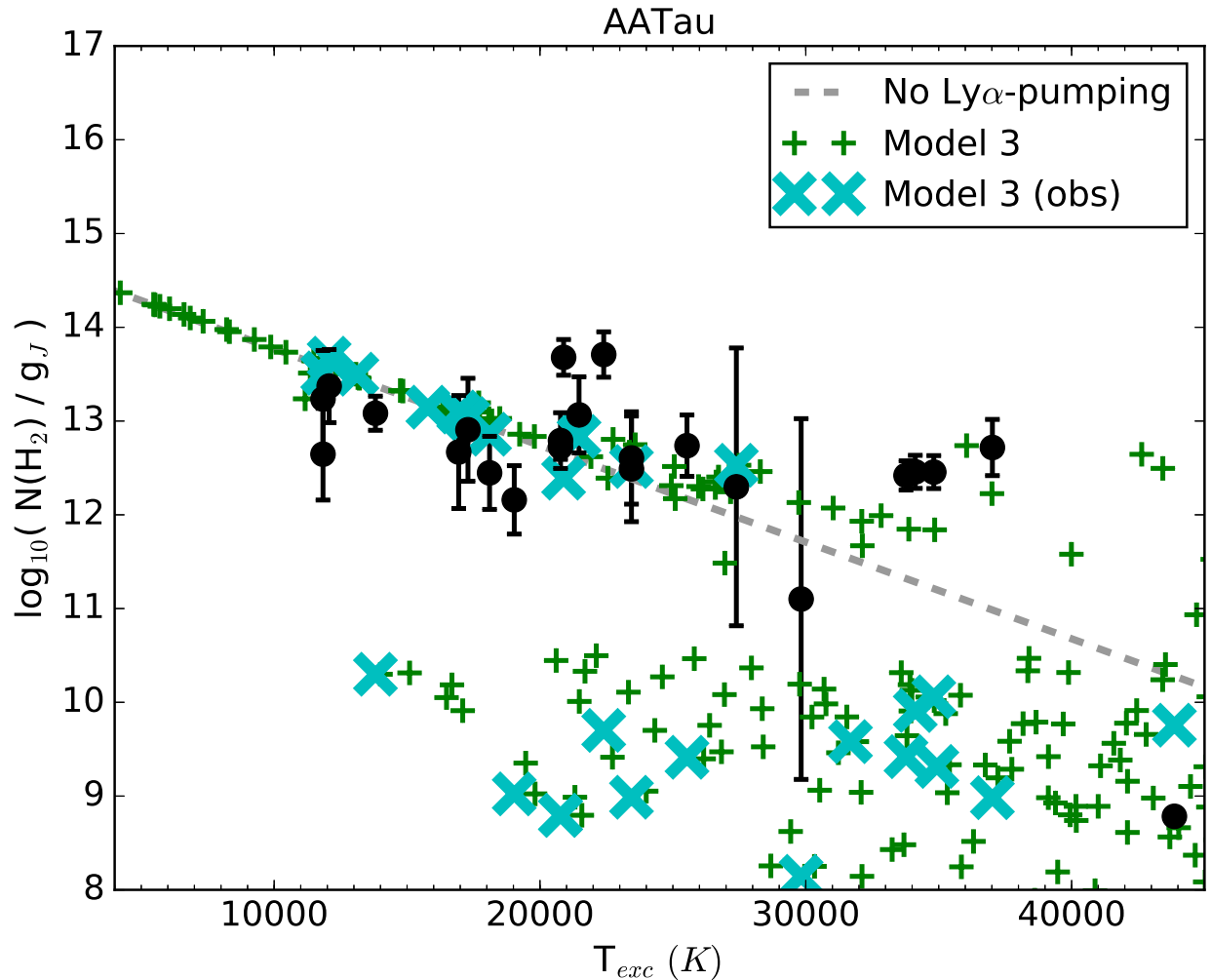


Figure 4. All rotation diagrams are presented here. Each H₂ ground state column density is weighed by its statistical weight, g_J . Model 1 attempts to fit one thermally-populated bulk H₂ population through all data points extracted from the *HST* data sets. Model 2 does the same as Model 1, but only for H₂ states with lower energy ground states ($E_{gr} \leq 1.5$ eV; $T_{exc} \leq 17,500$ K).

each modeled ro-vibration level with a green plus symbol, and we mark modeled ro-vibration levels which are probed in the observed Ly α wing(s) of the target with cyan crosses.

Fig. Set 4. Fitting Ly α -Pumping Models to Each H₂ Rotation Diagram

REFERENCES

- Abgrall, H., Roueff, E., Launay, F., Roncin, J. Y., & Subtil, J. L. 1993a, *A&AS*, 101, 273
— 1993b, *A&AS*, 101, 323
Ádámkóvics, M., Najita, J. R., & Glassgold, A. E. 2016, *ApJ*, 817, 82
Aikawa, Y. & Nomura, H. 2006, *ApJ*, 642, 1152
Akeson, R. L., Ciardi, D. R., van Belle, G. T., & Creech-Eakman, M. J. 2002, *ApJ*, 566, 1124
Alencar, S. H. P., Melo, C. H. F., Dullemond, C. P., Andersen, J., Batalha, C., Vaz, L. P. R., & Mathieu, R. D. 2003, *A&A*, 409, 1037
Alexander, R., Pascucci, I., Andrews, S., Armitage, P., & Cieza, L. 2014, *Protostars and Planets VI*, 475
Alexander, R. D. & Armitage, P. J. 2007, *MNRAS*, 375, 500
Alexander, R. D., Clarke, C. J., & Pringle, J. E. 2006, *MNRAS*, 369, 229
Andrews, S. M. & Williams, J. P. 2007, *ApJ*, 671, 1800
Andrews, S. M., Wilner, D. J., Espaillat, C., Hughes, A. M., Dullemond, C. P., McClure, M. K., Qi, C., & Brown, J. M. 2011, *ApJ*, 732, 42
Ardila, D. R., Basri, G., Walter, F. M., Valenti, J. A., & Johns-Krull, C. M. 2002, *ApJ*, 566, 1100

- Ardila, D. R., Herczeg, G. J., Gregory, S. G., Ingleby, L., France, K., Brown, A., Edwards, S., Johns-Krull, C., Linsky, J. L., Yang, H., Valenti, J. A., Abgrall, H., Alexander, R. D., Bergin, E., Bethell, T., Brown, J. M., Calvet, N., Espaillat, C., Hillenbrand, L. A., Hussain, G., Roueff, E., Schindhelm, E. R., & Walter, F. M. 2013, *ApJS*, 207, 1
- Armitage, P. J., Clarke, C. J., & Palla, F. 2003, *MNRAS*, 342, 1139
- Arulanantham, N. A., Herbst, W., Gilmore, M. S., Cauley, P. W., & Leggett, S. K. 2016, *ArXiv e-prints*
- Ayliffe, B. A. & Bate, M. R. 2010, *MNRAS*, 408, 876
- Ayres, T. R. 2010, *VizieR Online Data Catalog*, 218
- Bai, X.-N. 2016, *ApJ*, 821, 80
- Banzatti, A. & Pontoppidan, K. M. 2015, *ApJ*, 809, 167
- Bary, J. S., Weintraub, D. A., & Kastner, J. H. 2003, *ApJ*, 586, 1136
- Beck, T. L., Bary, J. S., Dutrey, A., Piétu, V., Guilloteau, S., Lubow, S. H., & Simon, M. 2012, *ApJ*, 754, 72
- Beckwith, S., Evans, II, N. J., Gatley, I., Gull, G., & Russell, R. W. 1983, *ApJ*, 264, 152
- Beckwith, S., Gatley, I., Matthews, K., & Neugebauer, G. 1978, *ApJL*, 223, L41
- Bergin, E., Calvet, N., Sitko, M. L., Abgrall, H., D'Alessio, P., Herczeg, G. J., Roueff, E., Qi, C., Lynch, D. K., Russell, R. W., Brafford, S. M., & Perry, R. B. 2004, *ApJL*, 614, L133
- Bertout, C., Basri, G., & Bouvier, J. 1988, *ApJ*, 330, 350
- Bertout, C., Robichon, N., & Arenou, F. 1999, *A&A*, 352, 574
- Bethell, T. J. & Bergin, E. A. 2011, *ApJ*, 739, 78
- Black, J. H. & Dalgarno, A. 1977, *ApJS*, 34, 405
- Böhm, T., Catala, C., Balona, L., & Carter, B. 2004, *A&A*, 427, 907
- Bouvier, J., Chelli, A., Allain, S., Carrasco, L., Costero, R., Cruz-Gonzalez, I., Dougados, C., Fernández, M., Martín, E. L., Ménard, F., Mennessier, C., Mujica, R., Recillas, E., Salas, L., Schmidt, G., & Wichmann, R. 1999, *A&A*, 349, 619
- Brown, J. M., Blake, G. A., Qi, C., Dullemond, C. P., Wilner, D. J., & Williams, J. P. 2009, *ApJ*, 704, 496
- Brown, J. M., Pontoppidan, K. M., van Dishoeck, E. F., Herczeg, G. J., Blake, G. A., & Smette, A. 2013, *ApJ*, 770, 94
- Calvet, N., D'Alessio, P., Hartmann, L., Wilner, D., Walsh, A., & Sitko, M. 2002, *ApJ*, 568, 1008
- Calvet, N., D'Alessio, P., Watson, D. M., Franco-Hernández, R., Furlan, E., Green, J., Sutter, P. M., Forrest, W. J., Hartmann, L., Uchida, K. I., Keller, L. D., Sargent, B., Najita, J., Herter, T. L., Barry, D. J., & Hall, P. 2005, *ApJL*, 630, L185
- Cartwright, D. C. & Drapatz, S. 1970, *A&A*, 4, 443
- Coffey, D., Bacciotti, F., Woitas, J., Ray, T. P., & Eislöffel, J. 2004, *ApJ*, 604, 758
- Comerón, F. & Fernández, M. 2010, *A&A*, 511, A10
- Comerón, F., Fernández, M., Baraffe, I., Neuhäuser, R., & Kaas, A. A. 2003, *A&A*, 406, 1001
- Correia, S., Zinnecker, H., Ratzka, T., & Sterzik, M. F. 2006, *A&A*, 459, 909
- Dalgarno, A. & Stephens, T. L. 1970, *ApJL*, 160, L107
- Danforth, C. W., Stocke, J. T., & Shull, J. M. 2010, *ApJ*, 710, 613
- Dodson-Robinson, S. E. & Salyk, C. 2011, *ApJ*, 738, 131
- Donehew, B. & Brittain, S. 2011, *AJ*, 141, 46
- Dong, R., Zhu, Z., & Whitney, B. 2015, *ApJ*, 809, 93
- Draine, B. T. 2011, *Physics of the Interstellar and Intergalactic Medium*
- Draine, B. T. & Bertoldi, F. 1996, *ApJ*, 468, 269
- Du, F. & Bergin, E. A. 2014, *ApJ*, 792, 2
- Dullemond, C. P., Hollenbach, D., Kamp, I., & D'Alessio, P. 2007, *Protostars and Planets V*, 555
- Dullemond, C. P. & Monnier, J. D. 2010, *ARA&A*, 48, 205
- Eisner, J. A., Hillenbrand, L. A., White, R. J., Bloom, J. S., Akeson, R. L., & Blake, C. H. 2007, *ApJ*, 669, 1072
- Espaillat, C., Calvet, N., D'Alessio, P., Bergin, E., Hartmann, L., Watson, D., Furlan, E., Najita, J., Forrest, W., McClure, M., Sargent, B., Bohac, C., & Harrold, S. T. 2007, *ApJL*, 664, L111
- Espaillat, C., Furlan, E., D'Alessio, P., Sargent, B., Nagel, E., Calvet, N., Watson, D. M., & Muzerolle, J. 2011, *ApJ*, 728, 49
- Fedele, D., van den Ancker, M. E., Henning, T., Jayawardhana, R., & Oliveira, J. M. 2010, *A&A*, 510, A72
- Feigelson, E. D., Lawson, W. A., & Garmire, G. P. 2003, *ApJ*, 599, 1207
- Ferreira, J., Dougados, C., & Cabrit, S. 2006, *A&A*, 453, 785
- Fleming, B., France, K., Lupu, R. E., & McCandliss, S. R. 2010, *ApJ*, 725, 159
- Foreman-Mackey, D., Hogg, D. W., Lang, D., & Goodman, J. 2013, *PASP*, 125, 306
- France, K., Burgh, E. B., Herczeg, G. J., Schindhelm, E., Yang, H., Abgrall, H., Roueff, E., Brown, A., Brown, J. M., & Linsky, J. L. 2012a, *ApJ*, 744, 22

- France, K., Herczeg, G. J., McJunkin, M., & Penton, S. V. 2014a, *ApJ*, 794, 160
- France, K., Roueff, E., & Abgrall, H. 2017, *ApJ*, *In Preparation*
- France, K., Schindhelm, E., Bergin, E. A., Roueff, E., & Abgrall, H. 2014b, *ApJ*, 784, 127
- France, K., Schindhelm, E., Burgh, E. B., Herczeg, G. J., Harper, G. M., Brown, A., Green, J. C., Linsky, J. L., Yang, H., Abgrall, H., Ardila, D. R., Bergin, E., Bethell, T., Brown, J. M., Calvet, N., Espaillat, C., Gregory, S. G., Hillenbrand, L. A., Hussain, G., Ingleby, L., Johns-Krull, C. M., Roueff, E., Valenti, J. A., & Walter, F. M. 2011, *ApJ*, 734, 31
- France, K., Schindhelm, E., Herczeg, G. J., Brown, A., Abgrall, H., Alexander, R. D., Bergin, E. A., Brown, J. M., Linsky, J. L., Roueff, E., & Yang, H. 2012b, *ApJ*, 756, 171
- Frisch, P. C., Dorschner, J. M., Geiss, J., Greenberg, J. M., Grün, E., Landgraf, M., Hoppe, P., Jones, A. P., Krätschmer, W., Linde, T. J., Morfill, G. E., Reach, W., Slavin, J. D., Svestka, J., Witt, A. N., & Zank, G. P. 1999, *ApJ*, 525, 492
- Furlan, E., Watson, D. M., McClure, M. K., Manoj, P., Espaillat, C., D'Alessio, P., Calvet, N., Kim, K. H., Sargent, B. A., Forrest, W. J., & Hartmann, L. 2009, *ApJ*, 703, 1964
- Garcia Lopez, R., Natta, A., Testi, L., & Habart, E. 2006, *A&A*, 459, 837
- Ghez, A. M., Neugebauer, G., & Matthews, K. 1993, *AJ*, 106, 2005
- Glassgold, A. E., Najita, J., & Igea, J. 2004, *ApJ*, 615, 972
- Glassgold, A. E. & Najita, J. R. 2001, in *Astronomical Society of the Pacific Conference Series*, Vol. 244, *Young Stars Near Earth: Progress and Prospects*, ed. R. Jayawardhana & T. Greene, 251
- Glassgold, A. E. & Najita, J. R. 2015, *ApJ*, 810, 125
- Gómez de Castro, A. I. 2009, *ApJL*, 698, L108
- Gorti, U. & Hollenbach, D. 2004, *ApJ*, 613, 424
- . 2009, *ApJ*, 690, 1539
- Gorti, U., Hollenbach, D., & Dullemond, C. P. 2015, *ApJ*, 804, 29
- Grady, C. A., Schneider, G., Sitko, M. L., Williger, G. M., Hamaguchi, K., Brittain, S. D., Ablordeppey, K., Apai, D., Beerman, L., Carpenter, W. J., Collins, K. A., Fukagawa, M., Hammel, H. B., Henning, T., Hines, D., Kimes, R., Lynch, D. K., Ménard, F., Pearson, R., Russell, R. W., Silverstone, M., Smith, P. S., Troutman, M., Wilner, D., Woodgate, B., & Clampin, M. 2009, *ApJ*, 699, 1822
- Grady, C. A., Woodgate, B., Torres, C. A. O., Henning, T., Apai, D., Rodmann, J., Wang, H., Stecklum, B., Linz, H., Williger, G. M., Brown, A., Wilkinson, E., Harper, G. M., Herczeg, G. J., Danks, A., Vieira, G. L., Malumuth, E., Collins, N. R., & Hill, R. S. 2004, *ApJ*, 608, 809
- Green, J. C., Froning, C. S., Osterman, S., Ebbets, D., Heap, S. H., Leitherer, C., Linsky, J. L., Savage, B. D., Sembach, K., Shull, J. M., Siegmund, O. H. W., Snow, T. P., Spencer, J., Stern, S. A., Stocke, J., Welsh, B., Béland, S., Burgh, E. B., Danforth, C., France, K., Keeney, B., McPhate, J., Penton, S. V., Andrews, J., Brownsberger, K., Morse, J., & Wilkinson, E. 2012, *ApJ*, 744, 60
- Güdel, M., Skinner, S. L., Mel'Nikov, S. Y., Audard, M., Telleschi, A., & Briggs, K. R. 2007, *A&A*, 468, 529
- Gullbring, E., Calvet, N., Muzerolle, J., & Hartmann, L. 2000, *ApJ*, 544, 927
- Gullbring, E., Hartmann, L., Briceño, C., & Calvet, N. 1998, *ApJ*, 492, 323
- Habart, E., Boulanger, F., Verstraete, L., Walmsley, C. M., & Pineau des Forêts, G. 2004, *A&A*, 414, 531
- Hartigan, P., Edwards, S., & Ghandour, L. 1995, *ApJ*, 452, 736
- Hartmann, L., Calvet, N., Gullbring, E., & D'Alessio, P. 1998, *ApJ*, 495, 385
- Hashimoto, J., Tamura, M., Muto, T., Kudo, T., Fukagawa, M., Fukue, T., Goto, M., Grady, C. A., Henning, T., Hodapp, K., Honda, M., Inutsuka, S., Kokubo, E., Knapp, G., McElwain, M. W., Momose, M., Ohashi, N., Okamoto, Y. K., Takami, M., Turner, E. L., Wisniewski, J., Janson, M., Abe, L., Brandner, W., Carson, J., Egner, S., Feldt, M., Golota, T., Guyon, O., Hayano, Y., Hayashi, M., Hayashi, S., Ishii, M., Kandori, R., Kusakabe, N., Matsuo, T., Mayama, S., Miyama, S., Morino, J.-I., Moro-Martin, A., Nishimura, T., Pyo, T.-S., Suto, H., Suzuki, R., Takato, N., Terada, H., Thalmann, C., Tomono, D., Watanabe, M., Yamada, T., Takami, H., & Usuda, T. 2011, *ApJL*, 729, L17
- Herczeg, G. J. & Hillenbrand, L. A. 2008, *ApJ*, 681, 594
- Herczeg, G. J., Linsky, J. L., Valenti, J. A., Johns-Krull, C. M., & Wood, B. E. 2002, *ApJ*, 572, 310
- Herczeg, G. J., Linsky, J. L., Walter, F. M., Gahm, G. F., & Johns-Krull, C. M. 2006, *ApJS*, 165, 256
- Herczeg, G. J., Walter, F. M., Linsky, J. L., Gahm, G. F., Ardila, D. R., Brown, A., Johns-Krull, C. M., Simon, M., & Valenti, J. A. 2005, *AJ*, 129, 2777
- Herczeg, G. J., Wood, B. E., Linsky, J. L., Valenti, J. A., & Johns-Krull, C. M. 2004, *ApJ*, 607, 369

- Hernández, J., Calvet, N., Briceño, C., Hartmann, L., Vivas, A. K., Muzerolle, J., Downes, J., Allen, L., & Gutermuth, R. 2007, *ApJ*, 671, 1784
- Herzberg, G. 1950, *Molecular spectra and molecular structure. Vol.1: Spectra of diatomic molecules*
- Hoadley, K., France, K., Alexander, R. D., McJunkin, M., & Schneider, P. C. 2015, *ApJ*, 812, 41
- Hollenbach, D. J. & Tielens, A. G. G. M. 1999, *Reviews of Modern Physics*, 71, 173
- Hughes, J., Hartigan, P., Krautter, J., & Kelemen, J. 1994, *AJ*, 108, 1071
- Ingleby, L., Calvet, N., Bergin, E., Herczeg, G., Brown, A., Alexander, R., Edwards, S., Espaillat, C., France, K., Gregory, S. G., Hillenbrand, L., Roueff, E., Valenti, J., Walter, F., Johns-Krull, C., Brown, J., Linsky, J., McClure, M., Ardila, D., Abgrall, H., Bethell, T., Hussain, G., & Yang, H. 2011, *ApJ*, 743, 105
- Jennings, D. E., Bragg, S. L., & Brault, J. W. 1984, *ApJL*, 282, L85
- Johns-Krull, C. M. & Valenti, J. A. 2001, *ApJ*, 561, 1060
- Johns-Krull, C. M., Valenti, J. A., & Linsky, J. L. 2000, *ApJ*, 539, 815
- Kamp, I. & Dullemond, C. P. 2004, *ApJ*, 615, 991
- Kamp, I., Dullemond, C. P., Hogerheijde, M., & Enriquez, J. E. 2005, in *IAU Symposium, Vol. 231, Astrochemistry: Recent Successes and Current Challenges*, ed. D. C. Lis, G. A. Blake, & E. Herbst, 377–386
- Kastner, J. H., Principe, D. A., Punzi, K., Stelzer, B., Gorti, U., Pascucci, I., & Argiroffi, C. 2016, *AJ*, 152, 3
- Kimble, R. A., Woodgate, B. E., Bowers, C. W., Kraemer, S. B., Kaiser, M. E., Gull, T. R., Heap, S. R., Danks, A. C., Boggess, A., Green, R. F., Hutchings, J. B., Jenkins, E. B., Joseph, C. L., Linsky, J. L., Maran, S. P., Moos, H. W., Roesler, F., Timothy, J. G., Weistrop, D. E., Grady, J. F., Loiacono, J. J., Brown, L. W., Brumfield, M. D., Content, D. A., Feinberg, L. D., Isaacs, M. N., Krebs, C. A., Krueger, V. L., Melcher, R. W., Rebar, F. J., Vitagliano, H. D., Yagelowich, J. J., Meyer, W. W., Hood, D. F., Argabright, V. S., Becker, S. I., Bottema, M., Breyer, R. R., Bybee, R. L., Christon, P. R., Delamere, A. W., Dorn, D. A., Downey, S., Driggers, P. A., Ebbets, D. C., Gallegos, J. S., Garner, H., Hetlinger, J. C., Lettieri, R. L., Ludtke, C. W., Michika, D., Nyquist, R., Rose, D. M., Stocker, R. B., Sullivan, J. F., Van Houten, C. N., Woodruff, R. A., Baum, S. A., Hartig, G. F., Balzano, V., Biagetti, C., Blades, J. C., Bohlin, R. C., Clampin, M., Doxsey, R., Ferguson, H. C., Goudfrooij, P., Hulbert, S. J., Kutina, R., McGrath, M., Lindler, D. J., Beck, T. L., Feggans, J. K., Plait, P. C., Sandoval, J. L., Hill, R. S., Collins, N. R., Cornett, R. H., Fowler, W. B., Hill, R. J., Landsman, W. B., Malumuth, E. M., Standley, C., Blouke, M., Gruszczak, A., Reed, R., Robinson, R. D., Valenti, J. A., & Wolfe, T. 1998, *ApJL*, 492, L83
- Kraus, A. L. & Hillenbrand, L. A. 2009, *ApJ*, 704, 531
- Kriss, G. A. 2011, *Improved Medium Resolution Line Spread Functions for COS FUV Spectra*, Tech. rep.
- Lawson, W. A., Crause, L. A., Mamajek, E. E., & Feigelson, E. D. 2001, *MNRAS*, 321, 57
- Lawson, W. A., Feigelson, E. D., & Huenemoerder, D. P. 1996, *MNRAS*, 280, 1071
- Lawson, W. A., Lyo, A.-R., & Muzerolle, J. 2004, *MNRAS*, 351, L39
- Levison, H. F., Kretke, K. A., & Duncan, M. J. 2015, *Nature*, 524, 322
- Lin, D. N. C. & Papaloizou, J. 1986, *ApJ*, 309, 846
- Loinard, L., Torres, R. M., Mioduszewski, A. J., Rodríguez, L. F., González-Lópezlira, R. A., Lachaume, R., Vázquez, V., & González, E. 2007, *ApJ*, 671, 546
- Lubow, S. H. & D'Angelo, G. 2006, *ApJ*, 641, 526
- Lubow, S. H., Seibert, M., & Artymowicz, P. 1999, *ApJ*, 526, 1001
- Luhman, K. L. 2004, *ApJ*, 617, 1216
- Lyo, A.-R., Ohashi, N., Qi, C., Wilner, D. J., & Su, Y.-N. 2011, *AJ*, 142, 151
- Mamajek, E. E., Lawson, W. A., & Feigelson, E. D. 1999, *PASA*, 16, 257
- Mandy, M. E. 2016, *ApJ*, 827, 62
- Mandy, M. E. & Martin, P. G. 1993, *ApJS*, 86, 199

- Markwardt, C. B. 2009, in *Astronomical Society of the Pacific Conference Series*, Vol. 411, *Astronomical Data Analysis Software and Systems XVIII*, ed. D. A. Bohlander, D. Durand, & P. Dowler, 251
- McCandliss, S. R. 2003, *PASP*, 115, 651
- McClure, M. K. and Bergin, E. A. and Cleeves, L. I. and van Dishoeck, E. F. and Blake, G. A. and Evans, II, N. J. and Green, J. D. and Henning, T. and Öberg, K. I. and Pontoppidan, K. M. and Salyk, C. A. 2016, *ApJ*, 831, 167
- McJunkin, M., France, K., Schindhelm, E., Herczeg, G., Schneider, P. C., & Brown, A. 2016, *ApJ*, 828, 69
- McJunkin, M., France, K., Schneider, P. C., Herczeg, G. J., Brown, A., Hillenbrand, L., Schindhelm, E., & Edwards, S. 2014, *ApJ*, 780, 150
- Nguyen, D. C., Brandeker, A., van Kerkwijk, M. H., & Jayawardhana, R. 2012, *ApJ*, 745, 119
- Nomura, H. 2004, *Ap&SS*, 292, 435
- Nomura, H., Aikawa, Y., Nakagawa, Y., & Millar, T. J. 2005, in *Protostars and Planets V Posters*, 8157
- Nomura, H., Aikawa, Y., Tsujimoto, M., Nakagawa, Y., & Millar, T. J. 2007, *ApJ*, 661, 334
- Nomura, H. & Millar, T. J. 2005, *A&A*, 438, 923
- Nomura, H. & Nakagawa, Y. 2006, *ApJ*, 640, 1099
- Öberg, K. I., van Dishoeck, E. F., Linnartz, H., & Andersson, S. 2010, *ApJ*, 718, 832
- Owen, J. E. 2016, *PASA*, 33, e005
- Owen, J. E., Ercolano, B., Clarke, C. J., & Alexander, R. D. 2010, *MNRAS*, 401, 1415
- Pontoppidan, K. M., Blake, G. A., van Dishoeck, E. F., Smette, A., Ireland, M. J., & Brown, J. 2008, *ApJ*, 684, 1323
- Prasad, S. S. & Huntress, Jr., W. T. 1980, *ApJS*, 43, 1
- Quast, G. R., Torres, C. A. O., de La Reza, R., da Silva, L., & Mayor, M. 2000, in *IAU Symposium*, Vol. 200, *IAU Symposium*, 28P
- Ramsay Howat, S. K. & Greaves, J. S. 2007, *MNRAS*, 379, 1658
- Ricci, L., Testi, L., Natta, A., Neri, R., Cabrit, S., & Herczeg, G. J. 2010, *A&A*, 512, A15
- Roberge, W. & Dalgarno, A. 1982, *ApJ*, 255, 176
- Rodriguez, D. R., Kastner, J. H., Wilner, D., & Qi, C. 2010, *ApJ*, 720, 1684
- Roncin, J.-Y. & Launay, F. 1995, in *Astronomical Society of the Pacific Conference Series*, Vol. 81, *Laboratory and Astronomical High Resolution Spectra*, ed. A. J. Sauval, R. Blomme, & N. Grevesse, 310
- Rosenfeld, K. A., Andrews, S. M., Wilner, D. J., & Stempels, H. C. 2012a, *ApJ*, 759, 119
- Rosenfeld, K. A., Qi, C., Andrews, S. M., Wilner, D. J., Corder, S. A., Dullemond, C. P., Lin, S.-Y., Hughes, A. M., D'Alessio, P., & Ho, P. T. P. 2012b, *ApJ*, 757, 129
- Rosenthal, D., Bertoldi, F., & Drapatz, S. 2000, *A&A*, 356, 705
- Salyk, C., Blake, G. A., Boogert, A. C. A., & Brown, J. M. 2011, *ApJ*, 743, 112
- Salyk, C., Pontoppidan, K. M., Blake, G. A., Lahuis, F., van Dishoeck, E. F., & Evans, II, N. J. 2008, *ApJL*, 676, L49
- Schindhelm, E., France, K., Herczeg, G. J., Bergin, E., Yang, H., Brown, A., Brown, J. M., Linsky, J. L., & Valenti, J. 2012, *ApJL*, 756, L23
- Schneider, P. C., France, K., Günther, H. M., Herczeg, G., Bouvier, J., Grankin, K., McJunkin, M., Robrade, J., & Schmitt, J. H. M. M. 2015, *A&A*
- Shull, J. M. & Beckwith, S. 1982, *ARA&A*, 20, 163
- Simon, M., Dutrey, A., & Guilloteau, S. 2000, *ApJ*, 545, 1034
- Smith, D., Adams, N. G., & Alge, E. 1982, *ApJ*, 263, 123
- Stecher, T. P. & Williams, D. A. 1967, *ApJL*, 149, L29
- Stempels, H. C., Gahm, G. F., & Petrov, P. P. 2007, *A&A*, 461, 253
- Stempels, H. C. & Piskunov, N. 2002, *A&A*, 391, 595
- Sternberg, A. 1989, *ApJ*, 347, 863
- Strom, K. M., Strom, S. E., Edwards, S., Cabrit, S., & Skrutskie, M. F. 1989, *AJ*, 97, 1451
- Takahashi, J., Masuda, K., & Nagaoka, M. 1999, *ApJ*, 520, 724
- Takeuchi, T. & Artymowicz, P. 2001, *ApJ*, 557, 990
- Tang, Y.-W., Guilloteau, S., Piétu, V., Dutrey, A., Ohashi, N., & Ho, P. T. P. 2012, *A&A*, 547, A84
- van Boekel, R., Min, M., Waters, L. B. F. M., de Koter, A., Dominik, C., van den Ancker, M. E., & Bouwman, J. 2005, *A&A*, 437, 189
- van den Ancker, M. E., de Winter, D., & Tjin A Djie, H. R. E. 1998, *A&A*, 330, 145
- van Leeuwen, F. 2007, *A&A*, 474, 653
- Walsh, C., Nomura, H., Millar, T. J., & Aikawa, Y. 2012, *ApJ*, 747, 114
- Walsh, C., Nomura, H., & van Dishoeck, E. 2015, *A&A*, 582, A88
- Webb, R. A., Zuckerman, B., Platais, I., Patience, J., White, R. J., Schwartz, M. J., & McCarthy, C. 1999, *ApJL*, 512, L63
- Weidenschilling, S. J. 1977, *MNRAS*, 180, 57
- White, R. J. & Ghez, A. M. 2001, *ApJ*, 556, 265
- Williams, D. & Murdin, P. 2000, *Physics of Molecules*

- Woitke, P., Dent, W. R. F., Thi, W.-F., Menard, F., Pinte, C., Duchene, G., Sandell, G., Lawson, W., & Kamp, I. 2013, in *Protostars and Planets VI Posters*, 13
- Woitke, P., Kamp, I., & Thi, W.-F. 2009, *A&A*, 501, 383
- Wolniewicz, L., Simbotin, I., & Dalgarno, A. 1998, *ApJS*, 115, 293
- Woodgate, B. E., Kimble, R. A., Bowers, C. W., Kraemer, S., Kaiser, M. E., Danks, A. C., Grady, J. F., Loiacono, J. J., Brumfield, M., Feinberg, L., Gull, T. R., Heap, S. R., Maran, S. P., Lindler, D., Hood, D., Meyer, W., Vanhouten, C., Argabright, V., Franka, S., Bybee, R., Dorn, D., Bottema, M., Woodruff, R., Michika, D., Sullivan, J., Hetlinger, J., Ludtke, C., Stocker, R., Delamere, A., Rose, D., Becker, I., Garner, H., Timothy, J. G., Blouke, M., Joseph, C. L., Hartig, G., Green, R. F., Jenkins, E. B., Linsky, J. L., Hutchings, J. B., Moos, H. W., Boggess, A., Roesler, F., & Weistrop, D. 1998, *PASP*, 110, 1183
- Yang, H., Linsky, J. L., & France, K. 2011, *ApJL*, 730, L10
- Youdin, A. N. 2011, *ApJ*, 731, 99
- Zhu, Z., Nelson, R. P., Hartmann, L., Espaillat, C., & Calvet, N. 2011, *ApJ*, 729, 47